International Journal of Earth Sciences (2020) 109:317–344
https://doi.org/10.1007/s00531-019-01804-9

ORIGINAL PAPER

Evidence of mingling between contrasting magmas in the Ribeirão do Óleo Pluton, Coastal Terrane and the tectonic implications on the Ribeira Belt, Brazil

Cláudia R. Passarelli[1] · **Sanjeet K. Verma**[2]

Received: 28 July 2019 / Accepted: 29 November 2019 / Published online: 1 January 2020

Abstract
Gneiss–migmatitic rocks and granites between the Cubatão and Itariri shear zones characterize the Mongaguá Complex-Coastal Terrane. Three major units are defined: (1) the Itariri Suite (IS) composed of monzogranites, granodiorites, tonalites, and locally gneiss–migmatitic rocks; (2) the Areado pluton composed of monzogranite and locally tonalite; and (3) the Ribeirão do Óleo Pluton mainly composed of monzogranites, which is the subject of this article. Combined field observations, petrography, Sr–Nd–Hf isotopes, U–Pb zircon data, and preliminary geochemical studies are presented for the Ribeirão do Óleo Pluton (ROP), intrusive in granite-gneisses of the IS. It is a plutonic association of weakly peraluminous, medium-to-high-K biotite monzogranites that surround microgranular intermediate enclaves, which are products of magma mingling. Different from the most examples of magma mingling described in the literature, the ROP mingling did not result from the intrusion of hot mafic magma into colder host felsic magma. Conversely, the emplacement of the monzogranite started most likely during the medium-to-final stage of crystallization of the quartz microdiorite. A detailed study of LA-ICP-MS U–Pb zircon ages, including zircon morphology and internal structure, was useful to determine more precisely the emplacement sequence and the relation between the units of the ROP. Intermediate and acid facies have Paleoproterozoic and Neoproterozoic inheritances, moreover a mixture of xenocrysts, antecrysts, and autocrysts, indicative of a complex evolution of the ROP. Several magma crystallization pulses are recorded at 655–624 Ma, 627–601 Ma, and 613–586 Ma. The negative εHf(t) ranging from − 17.26 to − 12.51 in monzogranites, εNd(t) values of − 10.66 to − 7.83 at $t=600$ Ma in both facies, $^{87}Sr/^{86}Sr$ of ca. 0.708 for the monzogranite and 0.706 for the quartz microdiorite indicate a strong crustal contribution in the genesis of intermediate and acid magmas of this pluton.

Keywords Ribeira Belt · Coastal Terrane · Magma mingling · LA-ICP-MS · Lu–Hf isotopes

Introduction

Expressive shear zones limit tectonic compartments with distinct lithologies, geochronology, and isotopic compositions of the Ribeira Belt (RB) in southeastern São Paulo State, which is a part of the Mantiqueira Province (MP) defined by Almeida et al. (1981, 2000). The largest tectonic unit of the MP (Fig. 1) is the RB that is generated from the closure of the Adamastor Ocean due to the interaction between the San Francisco, Paranapanema, Rio de la Plata, Luis Alves, Congo, and Kalahari cratons during Gondwana assembly (Fig. 1a).

The Coastal Terrane (CoT) of the RB (Fig. 1b) includes the Oriental Domain, which was defined by Heilbron et al. (2004, 2008) and Tupinambá et al. (2012), the Paranaguá/Iguape Domains (Cury et al. 2008; Passarelli et al. 2004),

Electronic supplementary material The online version of this article (https://doi.org/10.1007/s00531-019-01804-9) contains supplementary material, which is available to authorized users.

✉ Cláudia R. Passarelli
cr.passarelli@usp.br

[1] Instituto de Geociências, Universidade de São Paulo, Rua do Lago 562, Cidade Universitária, São Paulo, SP CEP 05508-080, Brazil

[2] División de Geociencias Aplicadas, Instituto Potosino de Investigación Científica y Tecnológica, Col. Lomas 4a Sec., C.P. 78216 San Luis Potosí, SLP, Mexico

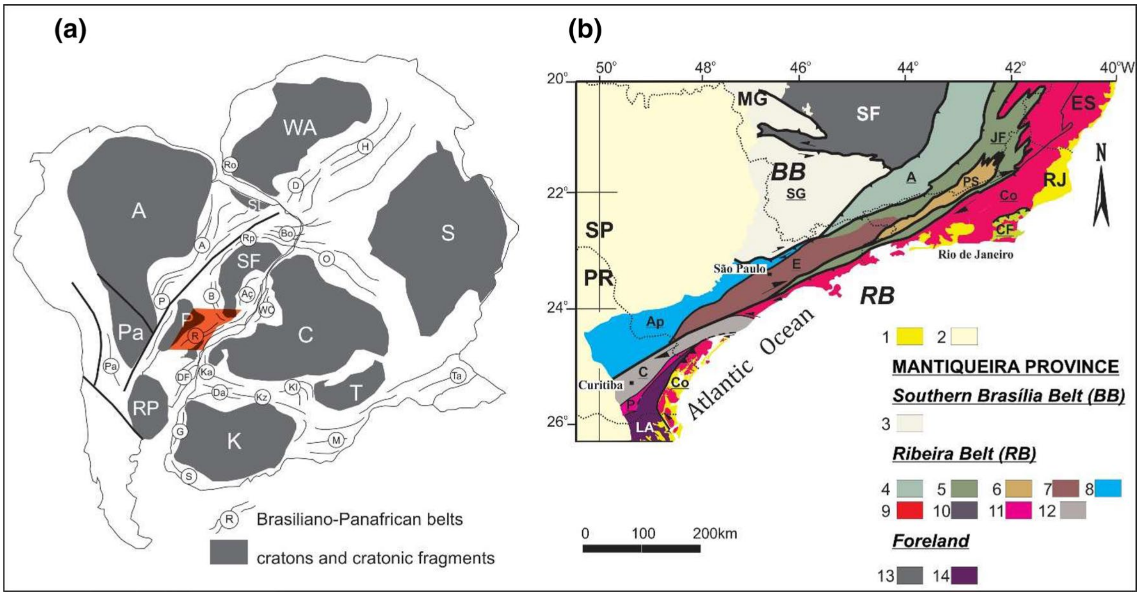

Fig. 1 **a** Reconstruction of West Gondwana after Heilbron et al. (2008), Vaughan and Pankhurst (2008), Frimmel et al. (2011) and Cordani et al. (2013). Cratons shown in grey: *A* Amazonia, *C* Congo, *K* Kalahari, *LA* Luis Alves, *P* Paranapanema, *SF* São Francisco, *WA* West Africa. Brasiliano–Panafrican belts (ringed): *Bo* Borborema, *Rp* Rio Preto, *A* Araguaia, *Aç* Araçuaí, *P* Paraguai, *B* Brasilía, *R* Ribeira, *DF* Dom Feliciano, *Pa* Pampean, *H* Hoggar, *D* Dahomey, *Ro* Rockelides, *O* Oubangides, *Ta* Tanzania, *WC* West Congo, *Ka* Kaoko, *Da* Damara, *K/Z* Katangan/Zambezi, *Kl* Katanga-Lufilian Arc, *M* Mozambique, *G* Gariep, *S* Saldania. Location of the northern Mantiqueira Province is shown. **b** General outline of the Northern Domain of the Mantiqueira Province (Brazil–Uruguay). Simplified from Basei et al. (1999, 2000), Heilbron et al. (2004), Tupinambá et al. (2007) and Passarelli et al. (2011). 1. Quaternary and Terciary sediments; 2. Paraná Basin (PB). Mantiqueira Province—Northern Domain: Brasília Belt (BB): 3. Socorro-Guaxupé nappe. Ribeira Belt (RB): 4. Andrelândia Terrane (A); 5. Juiz de Fora Terrane (JF); 6. Paraíba do Sul Terrane (PS); 7. Embu Terrane (E); 8. Apiaí Terrane (Ap); 9. Coastal Terrane (Co)—Coastal, Cambuci, Italva Domains, Rio Negro/Mongaguá/Paranaguá-Iguape Domains, Iguape Metassediments. 10. Cabo Frio Terrane (CF); 11. Piên Magmatic Arc (P); 12. Curitiba Terrane (C). Foreland units: 13. S. Francisco Craton and Cover (SF). 14. Luis Alves Terrane (LA). States of Brazil: ES-Espírito Santo, RJ-Rio de Janeiro, MG-Minas Gerais, SP-São Paulo, PR-Paraná

and the Mongaguá Domain (Passarelli et al. 2016). These areas are very important to understand the regional tectonics, because it offers an opportunity to discuss about the Curitiba and Paranaguá Domains (Siga Jr et al. 1995) that are situated in the south and belongs to the Oriental Domain (Heilbron et al. 2010) in the north.

The Mongaguá Complex (MC) initially named as Mongaguá Domain by Passarelli (2001) is composed of mainly gneiss–migmatitic and granitic rocks of Itariri Suite (IS) and Areado and ROP plutons, with Paleoproterozoic-to-Neoproterozoic ages (Passarelli et al. 2016). The term Complex is used here as defined by the International Stratigraphic Guide (Murphy and Salvador 1999) as a "lithostratigraphic unit composed of diverse types of any class or classes or rocks… and characterized by irregularly mixed lithology or by highly complicated structural relations". The MC is limited by Cubatão Shear Zone to the northwest and by the Itariri Shear Zone to the south.

The MC granitoids have been correlated with the Rio Negro magmatic arc in the Rio de Janeiro State and with Paranaguá Domain in the Paraná State (Passarelli et al. 2008, 2019). Magma mingling features have already been identified in the ROP by Passarelli (2001) and Passarelli et al. (2004). These authors provide some isotopic and U–Pb TIMS zircon data on granite of the ROP with strong isotope inheritance, showing inaccurate lower intercept ages around 580 Ma, TDM Nd age of 1729 Ma, εNd = − 10.7, and initial $^{87}Sr/^{86}Sr$ of 0.708. Preliminary LA-ICP-MS analyses on ROP granite give inconclusive ages around 560 Ma (Passarelli et al. 2016).

The main aim of this study is to report new petrographic, isotopic, and geochemical data of two lithotypes from the ROP to decipher their petrogenetic processes and possible emplacement environment.

Field evidence for magma mingling and isotopic mixing suggestion is presented where dioritic microgranular enclaves are surrounded by monzogranitic rocks. The interaction between two magmas of contrasting composition and physical properties generates several structures and textures preserved in the ROP. Textures can be interpreted with respect to effective magmatic processes at the time the magma chamber was active.

Geological context

The NE–SW-trending MP was generated during the Neoproterozoic Brasiliano–Panafricano Orogeny associated with the evolution of Western Gondwana assembly. Among the several belts diachronically developed in this province, the largest one is the RB that is situated in southeastern Brazil. It consists of several tectonic domains, limited either by thrust or by transpressive shear zones (Figs. 1b, 2) and a subduction-to-collisional belt developed consequently of the collision between the São Francisco, Paranapanema, Luís Alves, and Congo cratons and the assembly of West Gondwana during the Neoproterozoic (e.g., Brito Neves et al. 1999, 2014; Trouw et al. 2000; Campanha and Brito Neves 2004; Basei et al. 2010). The northern and central RB comprise the Occidental, Paraíba do Sul-Embú, Oriental (CoT or Serra do Mar Terrane) and Cabo Frio terranes (Campos Neto 2000; Heilbron et al. 2004; Schmitt et al. 2004; Tupinambá et al. 2012). Apiaí, Embú, and Curitiba terranes compose the southern RB (Campos Neto 2000; Basei et al. 2009; Siga Jr et al. 2011a, b), whereas the Lancinha-Cubatão and Itariri shear zones separate the supracrustal terranes to the north (Embu and Apiaí terranes) from the granite-gneissic migmatitic terranes to the south, including the CoT and Curitiba Terrane (CRT) (Fig. 1b). In addition, the Itariri Shear Zone (ISZ) separates the CRT from the MC-CoT (Fig. 2).

Coastal Terrane (CoT): central and northern RB

In the central RB, the CoT comprises the (1) Costeiro Complex, which contains orthogneisses and ortho-derived migmatite, para-derived migmatitic rocks, and amphibolite unit and calc-silicatic rocks; (2) syn-tectonic peraluminous and metaluminous granitic rocks, and (3) charnockitic rocks (Ubatuba Charnockite). The timing of diatexite melt crystallization is constrained at 584 Ma and 575 Ma with inherited cores of 770 Ma and 635 Ma. Amphibolitic rocks with ages between 650 and 550 Ma is interpreted as metamorphic events and ages of ca. 800–750 Ma as the crystallization age of the mafic protolith. The high-grade metasedimentary

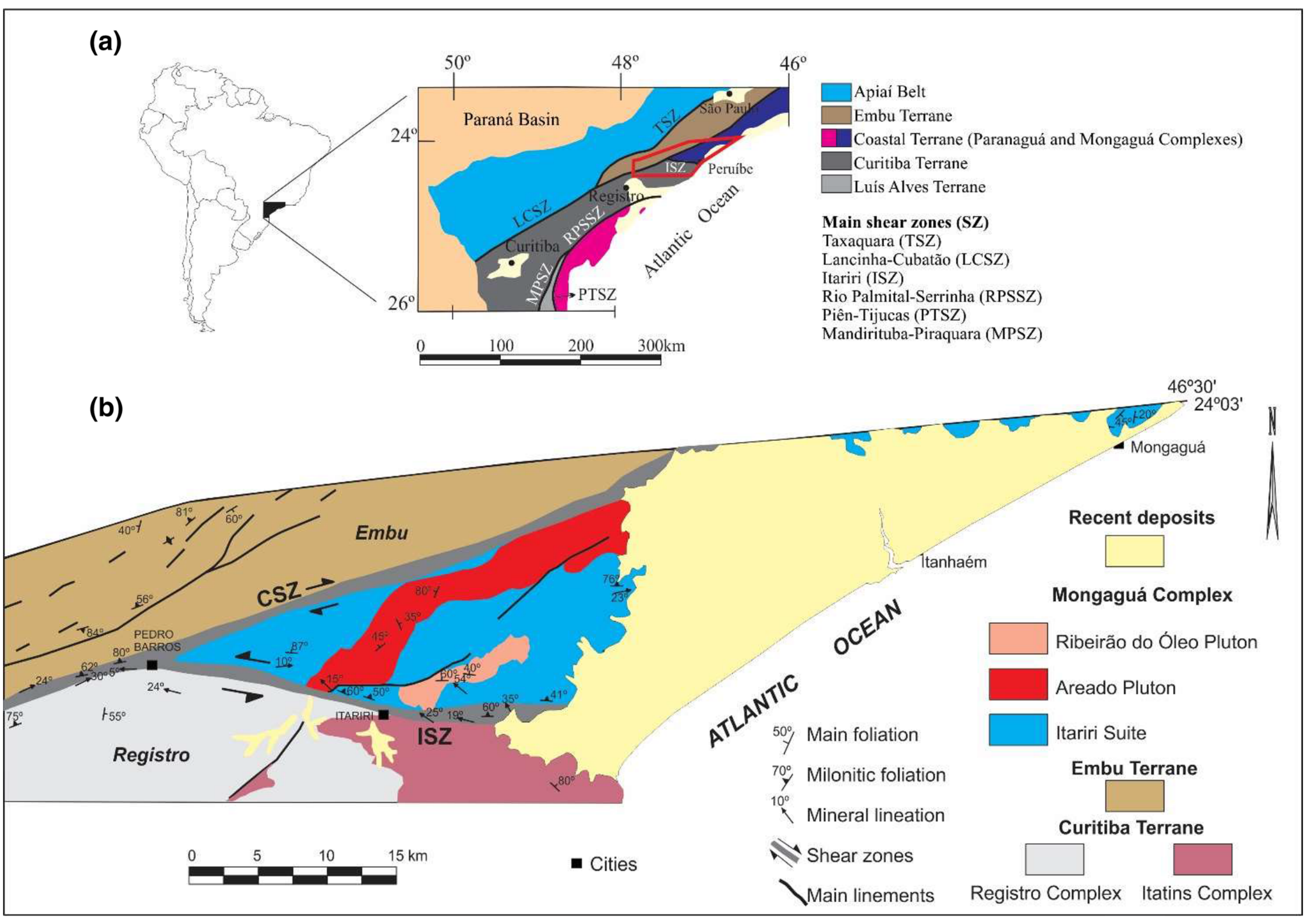

Fig. 2 **a** Tectonic sketch of the Mongaguá Complex (MC) adjacent terranes and main shear zones of the Southern RB with red polygon showing the location of the study area. **b** Simplified map of the MC with the main units: Itariri Suite, Areado, and Ribeirão do Óleo Plutons

rocks with maximum depositional age at 670–650 Ma; Ediacaran (587–562 Ma) I and S-type granites, late Ediacaran charnockitic rocks (ca. 560–565 Ma); Cambrian (ca. 500 Ma), quartz Monzonites, and Cretaceous alkaline rocks. (Janasi et al. 2003; Azevedo Sobrinho et al. 2011; Meira 2014; Meira et al. 2014, 2015).

In the Northern RB, the CoT, identified as Oriental Terrane (Heilbron et al. 2004, 2008, 2017), is made up of Tonian-to-Ediacaran juvenile intra-oceanic to immature continental arc-related rocks of the Costeiro Domain (Serra da Prata and Rio Negro complexes) and Neoproterozoic high-grade metasedimentary successions (Italva and São Fidélis Groups). The Costeiro domain, contains a distal passive margin succession of ca. 1000–760 Ma (lower units of the São Fidelis Group) intruded by the Neoproterozoic Rio Negro and Serra da Prata magmatic arcs of ca. 840–605 Ma. In a back arc setting, the São Fidélis and Italva basins deposited at ca. 840–605 Ma. Porphyritic syn-collisional granites (590–560 Ma), syn-collisional leucogranites and S-type to hybrid charnockites (ca. 580 Ma), late-collisional granites and charnockites (ca. 560 Ma), and post-collisional biotite granite (510–480 Ma) is also recognized in this terrane. A distinctive characteristic of this terrane is the absence of a Paleoproterozoic or older basement assemblage (Heilbron et al. 2017).

Coastal Terrane (CoT): southern RB

The MC is composed of granite and gneiss–migmatitic rocks including the IS and Areado and ROP plutons. The IS is mainly composed of monzogranite, granodiorite, and tonalite, some of which have a gneiss–migmatitic aspect. The Areado pluton contains monzogranite and some tonalitic rocks. The ROP is made of predominant granites and quartz microdiorites.

Isotopic data obtained on rocks of the IS, the Areado, and ROP plutons (Passarelli et al. 2014a) led to a better characterization of the MC (south of CoT), and revealed important differences with the lithotypes defined at the CoT to the north.

The IS includes medium-to-high-K monzogranites, granodiorites, and biotite tonalites, locally migmatitic. LA-ICP-MS geochronology of zircons provide U–Pb ages of 745 Ma in protomylonitic tonalite, and two age clusters of 640–630 Ma and 612 Ma in magmatic zircons and their overgrowths, respectively. Inherited cores provide ages of 2.2–2.1 Ga, 1.8 Ga, 1.2–1.1 Ga, and 790 Ma (Passarelli et al. 2014a). U–Pb monazite ages around 600 Ma indicate a thermal event in the area, which recorded in zircon rims. Paleoproterozoic ages around 2150 Ma, until undetected in this terrane, were found in the mesosome of migmatites, and represent minor basement remnants. The zircon data suggest that the IS granites crystallized in several magmatic pulses derived mainly from a Paleoproterozoic (2.2–1.8 Ga) source, which is a normal age for the South American basement rocks. On the other hand, the origin of Mesoproterozoic zircon ages (1200–1100 Ma) also observed in the Itariri rocks that are not so easy to explain since rocks with these ages have not so far been reported in any part of southern Brazil. The Namaqua rocks from southwestern Africa are the best candidates for the protoliths of the Itariri granites (Passarelli et al. 2016). The IS had been already associated with the 790–600 Ma Rio Negro Complex (Tupinambá et al. 2012) of Oriental Terrane in the central sector of the RB by Passarelli et al. (2004, 2008, 2011).

The record of Cryogenian magmatism (ca. 700 Ma) is also observed in the Areado pluton that presents local gneissic features. Paleoproterozoic basement (2150 Ma) is preserved as roof-pendants in the central part of the body. Inherited zircon cores in the Areado granite provide ages of 2.2–2.1 Ga, 1.8 Ga, and 860 Ma (Passarelli et al. 2016).

The ROP pluton presents well-characterized magma mingling features and apparently intrudes all units of the MC, although no contacts between the units were observed in the field. First, LA-ICP-MS analyses in the monzogranite of ROP provide ages around 560 Ma, and interpreted as the possible crystallization age of this body, although zircon with 610 Ma is also present (Passarelli et al. 2014b). Inherited zircon cores provide ages of 2.2–2.1 Ga, 700 Ma, and 645 Ma.

The study area is located in south-central portion of the MC, southern part of the RB. The ROP crop out north of the ISZ. It has a restricted expression in the area with exposure of around 9 km^2, and its long axis is oriented approximately N30E (Fig. 2). The monzogranite and diorite rocks of the ROP present an N80W to E–W main foliation with moderate dip (40°–60°) towards NE and contain a biotite and feldspar lineation with moderate plunges (54°) to N50W, possibly influenced by the ISZ kinematics (see Passarelli et al. 2011).

The IS, Areado, and ROP rocks have geochemical characteristics which point to the contribution of different crustal sources during the generation of these magmas. This finding is quite similar to studied rocks of southern Brazil.

Petrography of ROP

Petrographic studies were done on two main outcrops (K-54 and K-194) along the Oil Brook where the outcrops are slight or no weathered. The ROP was defined at northeast of the Itariri city where it is observed a clear interaction between acid and intermediate rocks. The acid rock is represented by biotite monzogranite medium grey-bluish coloring, finely foliated. These rocks have hypidiomorphic, inequigranular texture, and are fine-to-medium grained. The intermediate rocks of dioritic composition have dark grey in colour and are finely foliated as well.

The ROP shows evidence of both magmatic and solid-state flow. Structures of magmatic flow are well preserved, and are defined by macro- and microscopic structures such as aligned intermediate enclaves, euhedral K-feldspar megacrysts (Fig. 3a–c), and mafic minerals. Biotite crystals define a steeply plunging mineral lineation. The evidence of solid-state flow is better identified in thin sections, which is described latter.

Mingling structures consist of laterally discontinuous intermediate sheets with cuspate edges alternating with irregular elongate and flame-like shape enclave swarms (Fig. 3a–c). Normally near the magma's interaction, porphyritic textures with euhedral alkali feldspar megacrysts (10–45 mm) are found (Fig. 3c). Medium-to-coarse-grained quartz-feldspathic veins (Fig. 3d) and sheets form ptygmatic folds with axial plane roughly parallel to main foliation (Fig. 3e).

Biotite monzogranite (Fig. 4) composed of quartz, microcline, oligoclase, and biotite, whereas titanite, zircon, apatite, and rare sulphides as accessory minerals. Secondary minerals are sericite, epidote, chlorite, muscovite, and opaque oxide minerals. The colour index varies between 15 and 20. Foliation is defined by orientation of biotite crystals and the quartz segregations (Fig. 4a, sample K-54A; Fig. 4b, sample K-190A). Quartz crystals usually occur as polycrystalline aggregated with polygonised contacts. They tend to segregate in strips, but typically do not form ribbons. They do not show undulating extinction.

Microcline crystals are sometimes microperthitic and often are recrystallized (Fig. 4c, sample K-190A). Plagioclase crystals are commonly saussuritised. Biotite has light yellow-to-strongly reddish brown pleochroism. It alters to chlorite. Chlorite and muscovite crystals usually have well-developed shapes.

The evidence of solid-state flow in the monzogranite includes recrystallized aggregates of quartz and K-feldspar and elongated lenses of biotite (Fig. 4a, b).

Suggestion of a "submagmatic flow" (Paterson et al. 1989) or grain-supported flow (Vernon 2000) is evidenced by quartz-filled fractures in K-feldspar (Fig. 4c)

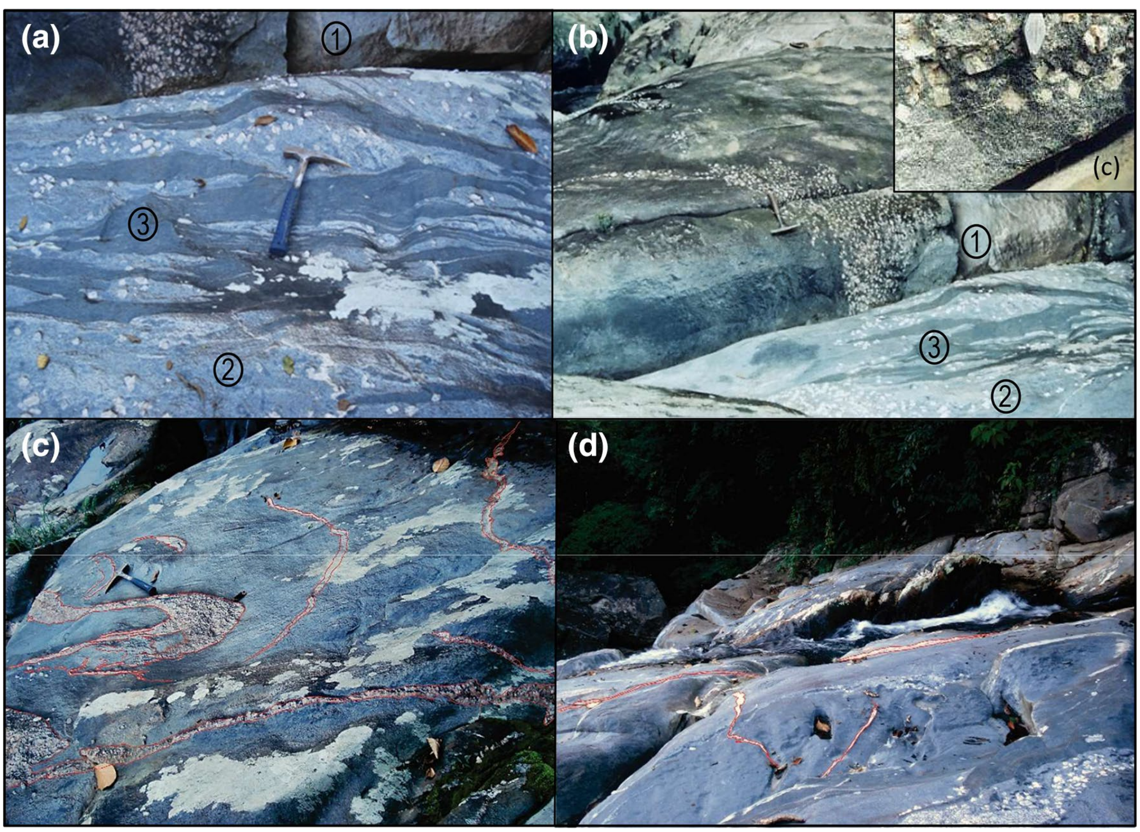

Fig. 3 Outcrop type of monzogranite and microdiorite mingling—Ribeirão do Óleo Pluton. **a** Note the higher concentration of K-feldspar phenocrysts nearby mafic material. **b** Mafic sheets with cuspate edges alternating with irregular elongate and flame-like shape enclave swarms and 'waterfall' of K-feldspar phenocrysts. **c** Detail of biotite monzogranite with euhedral K-feldspar phenocrysts. **d**, **e** Ptygmatic folds (highlighted) on medium-to-coarse-grained quartz-feldspathic veins. Location of samples for geochronology and geochemical studies is shown. Monzogranite: sample 1 (K-54A) and sample 2 (K-190A). Quartz microdiorite: sample 3 (K-190B)

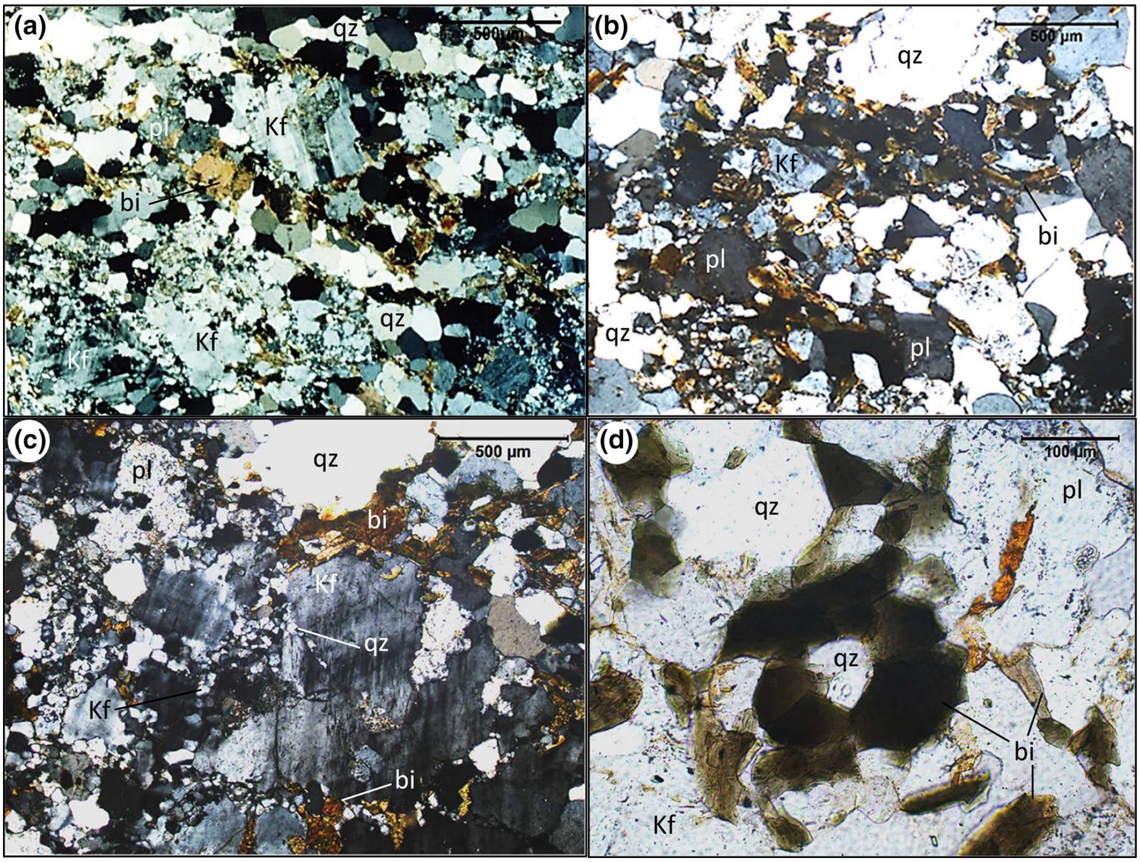

Fig. 4 Photomicrographs of Ribeirão do Óleo biotite monzogranite in XZ sections. **a**, **b** Foliation is expressed mainly by segregated bands of quartz and aligned biotite crystals. **c** K-feldspar recrystallization and fractures filled by quartz. **d** Quartz commonly supports coronas of biotite. Mineral abbreviations: bi, biotite; Kf, K-feldspar; pl, plagioclase; qz, quartz

and recrystallized K-feldspar with very discrete exsolution lamellae (Fig. 4c).

Some evidences of magma mingling in thin sections of granite samples are mantles or coronas (Fig. 4d, sample K-190A) that may be formed by diffusion-limited reactions in dissolution boundary layers (Stimac and Pearce 1992). Other evidences like a rounded and embayed crystal form are rare in quartz and K-feldspar.

Intermediate rock (sample 3, K-190B) is dioritic, composed of plagioclase, quartz, alkali feldspar, hornblende, and biotite, with titanite, zircon, and apatite as accessory phases. Epidote is the main secondary mineral. Colour index reached about 50%.

A folded foliation (Fig. 5a) is defined by mafic minerals and strong dynamic recrystallized quartz (Fig. 5b). This deformation led to deflection of mafic agglomerates, and to folding which affected biotite, hornblende, and sometimes epidote crystals (Fig. 5a). Myrmekites are common. Inclusions of biotite within hornblende and of hornblende within biotite are common substitution features.

The elongated intermediate enclaves enclosed in a finely foliated acid material possibly have deformed by solid-state deformation, due to a series of microstructures such as: (1) recrystallized aggregates of quartz and plagioclase (Fig. 5c); (2) myrmekite replacing K-feldspar, very local flame perthite, anastomosing foliations, shear bands (Fig. 5d); (3) undulose extinction, and recrystallization of minerals to finer aggregates (Fig. 5b, d); (4) irregular borders and lens-like shapes of hornblende crystals (Fig. 5a, b, e, f).

Mantles or coronas of hornblende and biotite (Fig. 5e), and mafic clots (Fig. 5f) in dioritic material also are typical textures whose origin can be explained in terms of magma mingling. However, suggestion of a "submagmatic flow" is not evidenced in this rock.

Cumulate layers of K-feldspar megacrysts

Near the contacts between quartz microdiorite and granite, there is a strong concentration of euhedral, centimetric phenocrysts of K-feldspar (Fig. 3a–c). Notably, the feldspars cumulate are clustered near the intermediate rock and are also present as xenocrysts in intermediate enclaves. Feldspar crystals may be partly or completely physically incorporated into enclaves before the enclaves

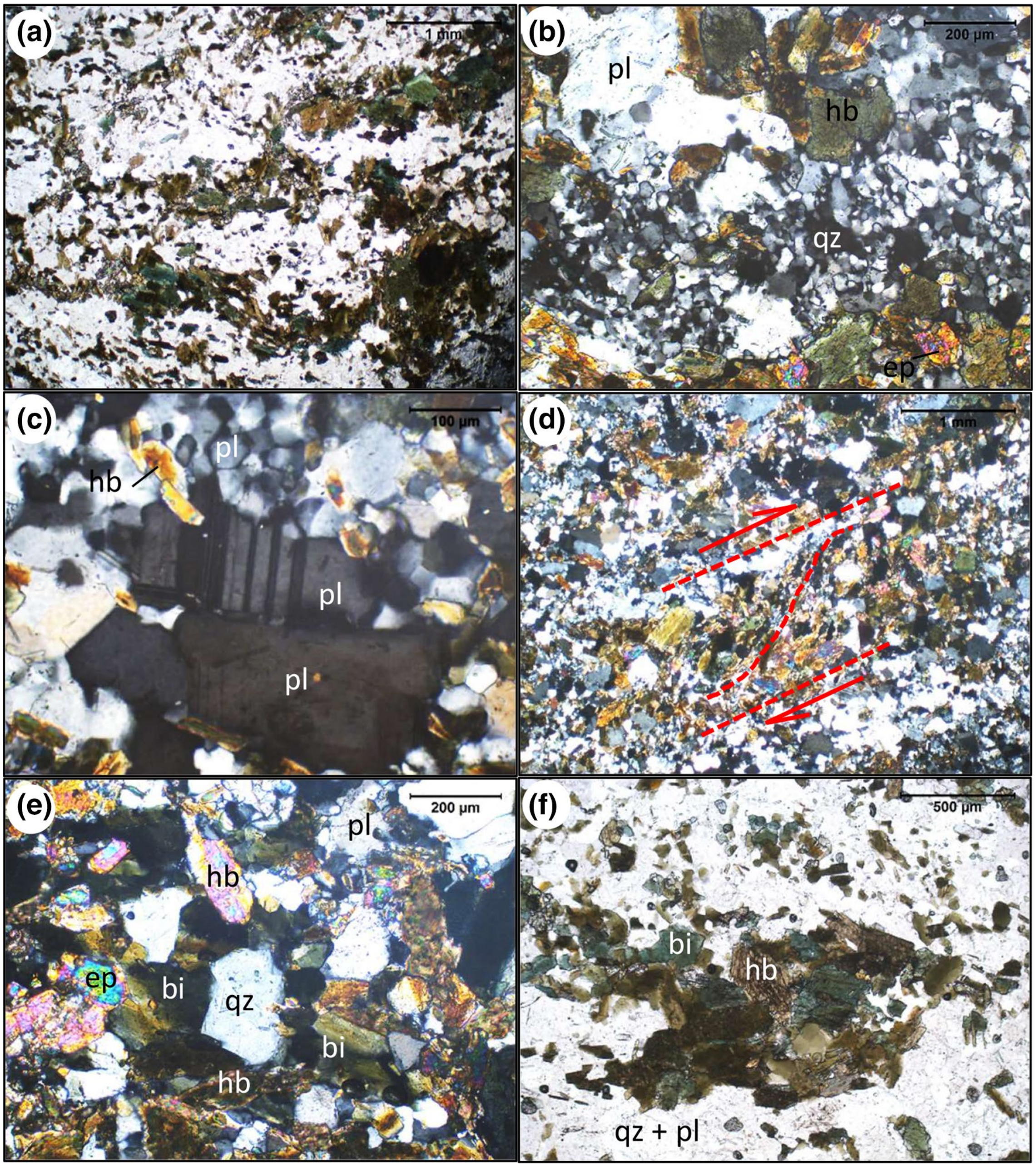

Fig. 5 Photomicrographs of Ribeirão do Óleo quartz microdiorite, sample 3 (K-190B). **a** Folded foliation. **b** Quartz dynamic recrystallization. **c** Recrystallization of plagioclase. **d** Shear bands with dextral movement. **e** Quartz crystal bordered by a corona of hornblende and biotite. **f** Mafic clot. Mineral abbreviations: hb, hornblende; bi, biotite; Kf, K-feldspar; pl, plagioclase; qz, quartz; ep-epidote

solidified (Vernon 1991), as shown in Fig. 3a representing incipient, local magma mingling that occurred just before consolidation of the accumulated enclaves (Vernon and Paterson 2006). Accumulation of crystals seems to be particularly common in granites showing evidence of magma mingling, which may be related to magma flows promoted by replacement of magma chambers (Vernon and Paterson 2006). In ROP, the evidences supporting physical accumulation of concentrations of K-feldspar megacrysts and not in situ growth (Paterson et al. 2005) include: (a) clustering of megacrysts in much greater modal proportions than is likely from the magma composition (Fig. 6); (b) imbrication of megacrysts (Fig. 6); (c) no evidence of adjustment around megacrysts even so many of them are in contact; (d) dike-like concentrations of megacrysts (Fig. 6) that in some places intrude other units with few-to-no megacrysts.

Fig. 6 Outcrop-type of monzogranite and microdiorite mingling—Ribeirão do Óleo Pluton. Thin feldspathic veins in mafic material (1), sometimes with complex folded structures (2). Concentration of medium–fine-grained K-feldspathic aggregates near the granite-diorite contact (3). K-feldspar cumulates with imbrication of phenocrysts up to 10 cm (4). Near of most K-feldspar cumulates, small enclaves or mafic clots in granite occur (5)

Analytical techniques

This work presents field and petrography, whole-rock geochemical and isotopic data, and LA-ICP-MS U–Pb and Lu–Hf data in zircon obtained from the intermediate and acid rocks from the ROP. All data were obtained at the facilities of the Núcleo de Apoio à Pesquisa (NAP)—Geoanalytic Laboratories—Geoscience Institute—São Paulo University, and of the Geochronological Research Centre (CPGeo), University of São Paulo, Brazil.

Mineral concentration

The concentration of the heavy mineral fraction for U–Pb analysis was conducted at the Mineral Separation Laboratory of the CPGeo, Brazil. The separation procedures were carried out as described by Passarelli et al. (2009).

LA-ICP-MS analyses

The procedures used for in situ analysis of U–Pb in zircon by LA-ICP-MS were described by Sato et al. (2009, 2012) and Matteini et al. (2010). The instruments used were an Excimer 193 nm laser coupled to a Thermo Scientific™ NEPTUNE™ MC-ICP-MS with a multi-collector array, installed at the CPGeo–IGc-USP laboratory. Analytical techniques for in situ Hf isotopic analyses in zircon have been described in detail by Wu et al. (2006) and Sato et al. (2009).

Between 30 and 50 zircon grains were dated per sample. The grains were mounted in 2.5 cm-diameter epoxy discs. The discs were polished sufficiently to expose the internal structures of the grains. All analyses are checked against zircon (GJ-1). Laser spot sizes used ranged from 20 to 32 µm (U–Pb analysis) to 47 µm (Hf analysis) and depth of crater ~ 10 µm. Each spot analysis took ca. 40 s. The complete procedures follow those outlined in Košler et al. (2002) and Košler and Sylvester (2003).

Isotope analyses were carried out on sites previously selected by cathodoluminescence (CL) microscopy studies to identify the best areas and beam spot sites in zircon grains. The analytical data were processed off-line using the data reduction program "R" (Siqueira et al. 2014). All final ages and plots were processed using the IsoplotEx software (Ludwig 2012).

The methodology for the determination of trace elements and REE in zircon grains performed in the NAP—Geoanalytic Laboratories with laser ablation associated with Quadrupole Inductively Coupled Plasma Mass Spectrometry (LA-Q-ICP-MS) is described in Andrade et al. (2014).

Whole-rock chemical and isotopic analyses

In total, three samples (two acid and one intermediate rock) were analysed. Bulk chemical X-ray fluorescence spectrometer analyses were performed using fused glass beads to determine the major and minor element compositions, and pressed pellets were used to determine the trace-element abundances. A computer program was used to calculate background, interference, mass absorption, and root mean square. 169 and 114 reference samples were used for calibration of major and minor elements, respectively, as specified in Mori et al. (1999). Quality control used one or two standards used in the calibration, but treated as unknowns. Trace-element and REE abundances were determined by the ICP-MS and the analytical procedure described by Navarro et al. (2008).

A Finnigan MAT 262 multi-collector thermal ionization mass spectrometer (TIMS) was used to obtain Sr–Nd and Rb–Sr whole-rock isotope analyses at the CPGeo-IGc-USP. Nd crustal residence ages (TDM) were calculated following the depleted mantle model of DePaolo (1981), and a two-stage Nd isotope evolution model was used for the calculation of the TDM of DePaolo et al. (1991). εNd(t) values were calculated by using U–Pb zircon ages. Neodymium crustal residence ages (TDM) were calculated following the depleted mantle model of DePaolo (1981), and a two-stage Nd isotope evolution model was used for the calculation of the TDM of DePaolo et al. (1991). εNd(t) values were calculated using U–Pb zircon ages.

Results

Major and trace elements

A total of three samples (1 quartz microdiorite and 2 monzogranite) from the ROP were collected for whole-rock major and trace-element composition analyses. The results are given in Table S1. The quartz microdiorite has SiO_2 contents 59.10 wt%, K_2O contents 3.33 wt%, Na_2O_3 contents 3.69 wt%, CaO contents 5.42 wt%, and Al_2O_3 contents 15.31 wt%, exhibiting a metaluminous feature (A/CNK = 0.78 (Fig. 7a). In addition, quartz microdiorite is characterized by high MgO contents 4.06 wt% with Mg-number (Mg#) of 55 [Mg# = 100 × (Mg^{2+}/(Mg^{2+} + Fe^{2+}))]. The monzogranite samples record values of SiO_2 = 66.35–70.52 wt%, K_2O = 3.56–3.92 wt%, Na_2O_3 = 4.16–4.53 wt%, MgO = 1.26–1.33 wt%, and Mg# = 42.19–47.77. They display peraluminous feature (A/CNK = 1.00–1.04) (Fig. 7a). All the samples plot in the subalkaline series and discriminated as granite and diorite in the total vs alkali (TAS) diagram (Fig. 7b) and high-K calc-alkaline series in SiO_2–Ka_2O diagram (Fig. 7c).

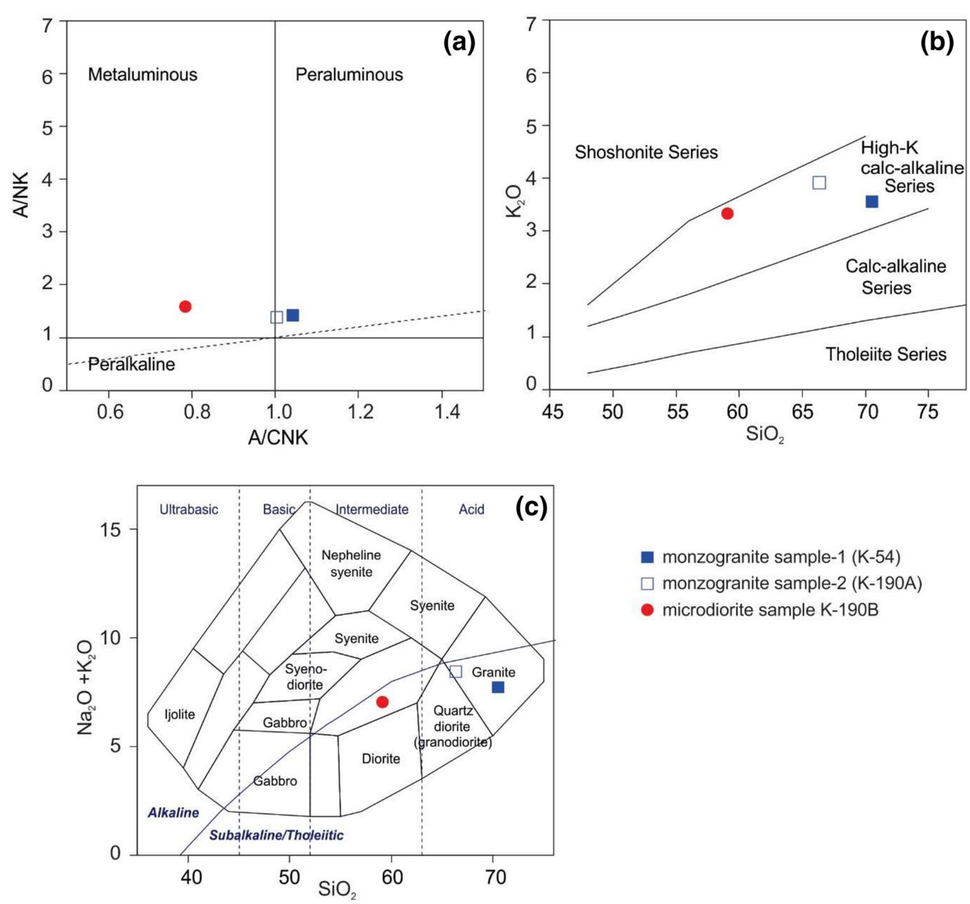

Fig. 7 **a** A/CNK × A/NK diagram after Maniar and Piccoli (1989), based on the Shand's index; **b** SiO_2 × K_2O after Peccerillo and Taylor (1976); **c** TAS classification diagram of the granitoids using the classification of Cox et al. (1979)

The chondrite-normalized rare-earth element (REE; McDonough and Sun 1995) plots of the new data (Table S1) are shown in Fig. 8. The quartz microdiorite displays enrichment in light REE (LREE; $(La/Sm)_{CN} = 5.56$) and a depleted HREE patterns $(Gd/Yb)_N = 3.52$), with no Eu anomalies (Fig. 8a). The monzogranite samples also show enrichment in LREE (Fig. 8b; $(La/Sm)_{CN} = 5.52–6.64$) and a depleted HREE patterns $(Gd/Yb)_N = 2.94–3.64$), which also show no Eu anomalies (Fig. 8b). On the primitive mantle-normalized spidergram (Fig. 8b), the samples exhibit high concentrations of Rb, Th, and Pb. They also show characteristics of negative anomalies of Nb, P, and Ti, which might be associated with the magmatic differentiation of plagioclase residual.

Sm–Nd and Rb–Sr isotopic data

The whole-rock Nd and Sr isotope compositions are listed in Tables S2 and S3 for the Ribeirão do Óleo Pluton. The two monzogranite samples have relatively consistent $^{143}Nd/^{144}Nd$ ratios ranging from 0.5117 to 0.5118, whereas one dioritic sample shows 0.5118, corresponding to $_{\varepsilon Nd}(t)$ values of − 7.83 to − 10.66 at t = 600 Ma. In addition, $^{87}Sr/^{86}Sr$ initial ratios display the values of ca. 0.708 for the monzogranite and 0.706 for the quartz microdiorite.

Zircon U–Pb (LA-ICP-MS) geochronology

Zircon crystals were studied using conventional optical microscopy and CL imaging. All CL images were produced from a split screen on an FEI Quanta 250 Scanning Electron Microscope (SEM) and XMAX CL detector (Oxford Instruments) at the Laboratory of High-Resolution Geochronology of the Institute of Geosciences of the University of São Paulo (GeoLab-IGc-USP). For description details of the optical and electronic imagery, see Sato et al. (2014).

Usually, bright CL image indicates U-poor domains with a well-ordered crystal lattice and dark CL image indicates U-rich domains. Primary internal zircon structures can be observed by the CL images, but important secondary features were also observed in zircons from Ribeirão do Óleo granite.

External and internal morphology

The zircon crystals of the ROP monzogranite are normally transparent, sub-euhedral and short-to-long prismatic grains (2:1–7:1) with an average 3:1. The pyramidal faces are under-developed (Fig. 9a–c). Inclusions of other minerals and some degree of fracturing are very common. In optical microscopy, magmatic zonation can be observed through conspicuous growth zones (Fig. 9c).

The zircon crystals of the ROP microdiorite are normally transparent, sub-euhedral and medium-to-long prismatic grains with an average 4:1. The pyramidal faces are under-developed (Fig. 9d, e). Widespread inclusions and fracturing occur. In optical microscopy, magmatic zonation also can be observed through visible growth zones (Fig. 9e).

The most common pattern in analysed crystals identified by CL imaging is the oscillatory/sector zoning that represents the heterogeneous distribution of trace elements (Hoskin 2000) and presence of possibly xenocrystic inherited cores. Figure 10 shows selected zircon CL images from monzogranite and quartz microdiorite, respectively.

As shown in Fig. 10a, zircons from the monzogranite (sample 1—K-54A) display growth zoning (oscillatory or sector zoned), usually darker (weak CL) than the inherited core (exception of zircon 14). Blurred primary zones are also common. In the sample 2—K-190A, the inherited core is either brighter or darker than rims (Fig. 10b). Rare homogeneously textured zircon crystals occurred (zircon 20 Fig. 10a; zircons 1, 3, 16 Fig. 10b). Presence of transgressive zones of recrystallization, local development of convolute zoning, and complex growth zoning with possible local intermediate resorption in zircon occur in the inherited cores (zircons 5, 11, 12, 13, 24, 25 and 30, Fig. 10a; zircons 4, 8, 9, 16, 17, 18, 21, Fig. 10b).

Mostly of the zircon crystals of the quartz microdiorite exhibit low CL intensity (Fig. 10c) with exception of xenocrysts or inherited cores (see explanation on item 5.3.2). Magmatic growth oscillatory zoning, blurred primary zones

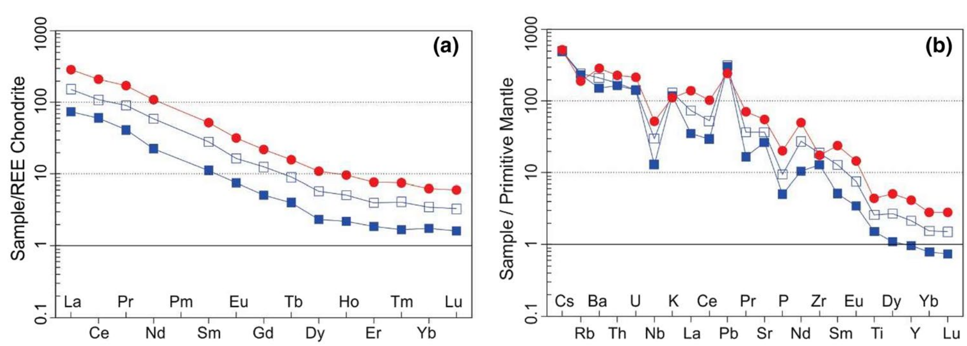

Fig. 8 **a** Chondrite-normalized (Nakamura 1974) REE distribution patterns; **b** primitive mantle-normalized multi-element plot (Sun and McDonough 1989) of ROP samples. Legend is the same of Fig. 7

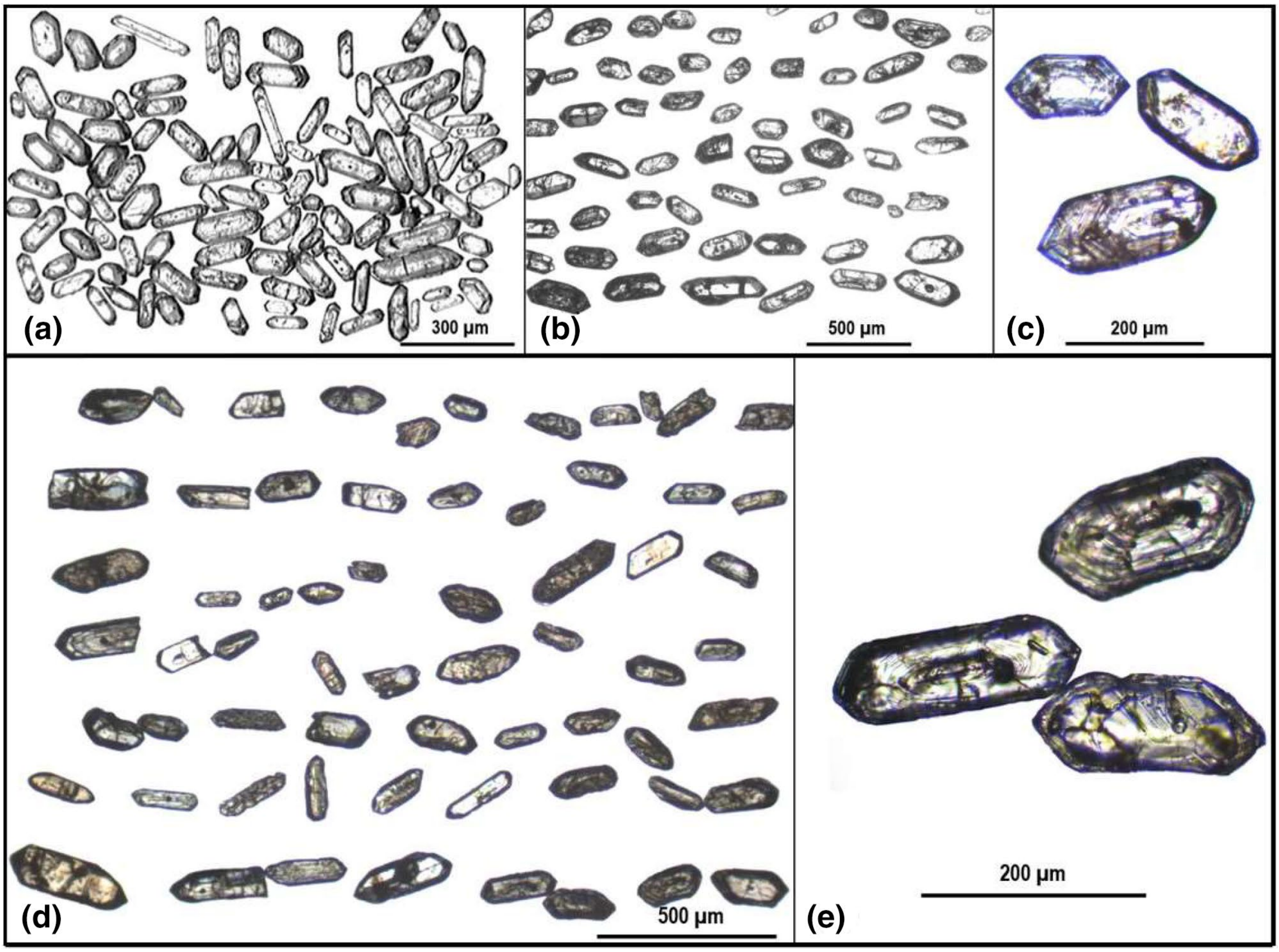

Fig. 9 Transmitted light images showing external morphology variations of zircon crystals from biotite monzogranite (**a**–**c**) and microdiorite (**d**, **e**) of ROP. Monzogranite: **a** sample 1 (K-54A); **b** sample 2 (K-190A); **c** detail of zircon crystals with magmatic zonation (sample 2, K-190A). Microdiorite: **d** sample 3 (K-190B). **e** Detail of zircon crystals with magmatic zonation

(zircons 1, 2, 3, 4, 6, 10, 12, 16, 20, Fig. 10c), with presence of possibly xenocrystic inherited cores (zircons 6, 8, 9, 11, 12, 15, 16, 20, Fig. 10c), and transgressive zones of recrystallization (zircons 1, 3, 6, 16, Fig. 10c) are observed. Development of local convolute zoning is rare (zircon 1 and 11, Fig. 10c). Homogeneously textured zircon crystals are not rare (zircons 8, 12 and 16, Fig. 10c). Low-luminescent metamorphic rim is present in samples 2 and 3 (Fig. 10b, c).

U–Pb zircon dating

The result of the LA-ICP-MS U–Pb analysis is given in Tables 1, 2 and 3. The data are presented as Concordia age with 1 sigma, decay-constant errors, MSWD and probability (of concordance) are indicated. The U–Pb analyses were performed in two samples of the foliated biotite monzogranite (sample 1 and 2—Fig. 3) and in one sample of the quartz microdiorite enclaves (sample 3—Fig. 3). Concordant zircon age dispersion is observed in both rocks of the ROP and only with the joint investigation with the CL images of the analysed zircon grains was possible to interpret the different sets of concordant ages. Only analyses with sub-concordant passing a < 10% discordancy test were considered. Systematic age variation between cores and rims is clearly shown in analysed zircon grains.

Monzogranite Thirty-three zircons of sample 1 (K-54A) have a relatively narrow range in Th/U ratios (0.24–1.07) but a wide range in Th (55–2613 ppm) and U (74–4019 ppm) contents (Table 1). This sample is located a quite distance (ca. 3 meters) from the enclaves (Fig. 3) and displays an interval between ca. 700 and 550 Ma of concordant ages (Fig. 11a, b). Two different sets of data of spot analyses with oscillatory zoning provide ages of 586 Ma (zircons 16, 27 and 28 Fig. 10a) and 613 Ma (zircons 4, 6 and 20 Fig. 10a) are interpreted as autocrysts and antecrysts, respectively.

Cores (possibly xenocrysts) (spots 1.1, 7.1, 8.1, 9.1 Fig. 10a) provide ages of 645 and 690 Ma, where spot 8.1

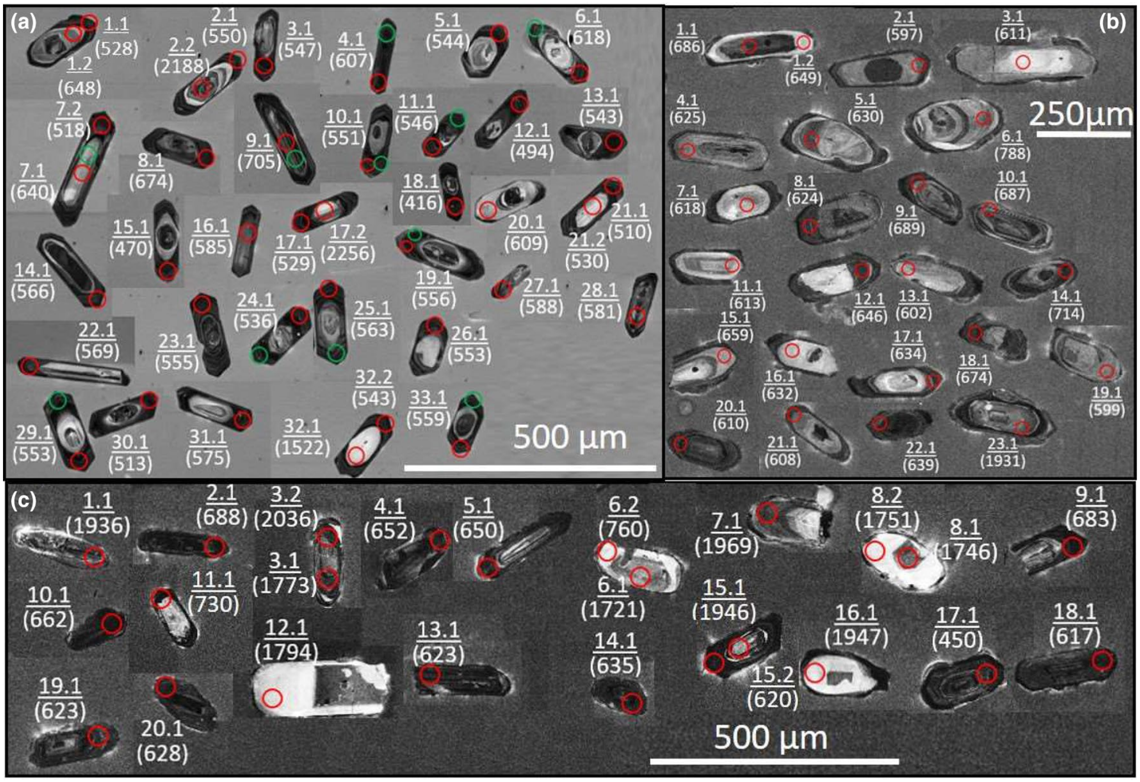

Fig. 10 Cathodoluminescence (CL) images of zircon grains: spot locations for U–Pb (red circles), Hf (green circles) analyses, $^{206}Pb/^{238}U$ ages in Ma are shown. The underlined numbers indicating the spots are shown. Zircon internal structures are discussed in the text. **a** Biotite monzogranite sample 1 (K-54A); **b** biotite monzogranite sample 2 (K-190A); **c** quartz microdiorite sample 3 (K-190B)

although located on the edge of the crystal must have caught in depth part of the zircon core. In addition, inherited cores of Paleoproterozoic age of 2.21 ± 0.42 Ga (Fig. 11a) were dated (spots 2.2 and 17.2—Fig. 10a).

The larger set of data provide a Concordia age of 556 Ma (Fig. 11b), although this age corresponds to a range of concordant ages between 570 and 540 Ma. This interval corresponds to analyses on: darker rims, usually with high Th and U contents, with mainly sector zoning and probably represents late and/or hydrothermal zircons.

The second dated sample (K-190A) is located in an area closer to the intermediate enclaves (Fig. 3). Twenty-three zircons of sample 2 have a relatively wide range in Th (24–605 ppm) and U (48–637 ppm) contents, but a relatively narrow range in Th/U ratios (0.29–1.24). The exceptions on Th/U ratios between 0.02 and 0.12 (spots 1.2, 8.1, 9.1, 12.1, 14.1 and 18.1) are discussed later (Table 2).

An interval between ca. 650 and 600 Ma of concordant ages is record (Fig. 11c). However, based on CL images, four different groups of ages can be identified: 601 Ma, 613 Ma, 627 Ma, and 647 Ma.

The crystallization age 601 ± 4 Ma (Fig. 11c) of the sample 2 is defined by the autocrysts with magmatic oscillatory zoned domains (spots 2.1, 19.1, 21.1 Fig. 10b).

Relative homogeneous zircon cores with high CL intensity (spots 3.1, 7.7, 11.1, 13.1, 16.1—Fig. 10b) provide an age of 613 ± 5 Ma (Fig. 11c). Darker zoned mantle (spots 5.1, 8.1, 17.1, 20.1, 22.1—Fig. 10b) of possibly zircon cores provides an age of 627 ± 2 Ma.

The age of 682 ± 3 Ma was obtained mainly on sector zoning rims and mantles (spots 9.1, 10.1, 14.1, 18.1—Fig. 10b) and in one zircon core (spot 1.1—Fig. 10b). Unzone cores enclosed by planar zoned or unzone mantles (spots 1.2, 12.1 and 15.1—Fig. 10b), normally with low Th/U values, with thin discrete darker non-dated rims provide an age of 647 ± 4 Ma, probably from a late-stage magmatic or metamorphic episode of the 682 Ma xenocrysts.

Xenocryst with age around 788 Ma shows heterogeneous core (spot 6.1—Fig. 10b) surrounded by sector and oscillatory zoning mantle with fine darker rim. Inherited nuclei with discordant Paleoproterozoic age were dated (spot 23.1—Fig. 10b).

Quartz microdiorite The 20 analysed zircons of sample 3 (K-190B) can be divided into main three groups regarding the CL intensity and Th and U contents: (1) xenocrysts with normally high CL intensity (grains 1, 3, 6, 7, 8, 12, and 16—Fig. 10c) with a relatively narrow range in Th (16–

Table 1 Results of U–Pb LA-ICP-MS dating of zircons on biotite monzogranite of ROP—sample 1 (K-54A)

Spot	Contents (µg/g) %				Isotopic ratios							Isotopic ages (Ma)						Conc %	
	Th	U	Th/U	C Pb	$^{207}Pb/^{235}U$	1σ	$^{206}Pb/^{238}U$	1σ	ρ	$^{207}Pb/^{206}Pb$	1σ	$T_{206/238}$	1σ	$T_{207/235}$	1σ	$T_{207/206}$	1σ	1	2
1.1	434.8	985.5	0.44	3.03	0.6872	0.0104	0.0853	0.0014	1.00	0.0601	0.0007	528	8	531	6	626	27	99	88
1.2	61.9	213.4	0.29	0.39	0.8904	0.0111	0.1058	0.0016	1.00	0.0606	0.0007	648	9	647	6	626	25	100	105
2.1	194.8	610.7	0.32	2.21	0.7091	0.0118	0.0891	0.0014	0.94	0.0597	0.0009	550	8	544	7	587	33	101	94
2.2	250.7	305.3	0.82	0.05	7.4006	0.1380	0.4041	0.0079	1.00	0.1431	0.0019	2188	36	2161	17	626	22	101	97
3.1	211.5	549.1	0.39	3.92	0.7447	0.0111	0.0886	0.0014	1.00	0.0622	0.0009	547	8	565	6	626	30	97	81
4.1	253.9	1001.3	0.25	1.58	0.8181	0.0115	0.0987	0.0016	1.00	0.0606	0.0009	607	9	607	6	626	31	100	98
5.1	638.5	1232.9	0.52	0.91	0.7198	0.0095	0.0881	0.0014	1.00	0.0592	0.0007	544	8	551	6	570	26	99	96
6.1	193.7	649.9	0.30	0.81	0.8503	0.0144	0.1006	0.0017	0.98	0.0607	0.0009	618	10	625	8	626	32	99	100
7.1	2612.8	3178.6	0.82	5.76	0.8612	0.0125	0.1043	0.0018	1.00	0.0612	0.0007	640	11	631	7	626	25	101	100
7.2	473.4	1315.4	0.36	1.93	0.6764	0.0101	0.0837	0.0014	1.00	0.0596	0.0007	518	8	525	6	626	26	99	89
8.1	1180.9	1105.8	1.07	6.20	0.9367	0.0126	0.1103	0.0018	1.00	0.0623	0.0007	674	10	671	7	626	25	100	99
9.1	54.5	231.6	0.24	0.00	0.9704	0.0133	0.1156	0.0018	1.00	0.0630	0.0007	705	11	689	7	626	25	102	100
10.1	660.7	1364.9	0.48	7.53	0.7355	0.0094	0.0893	0.0014	1.00	0.0600	0.0007	551	8	560	6	598	26	98	92
11.1	597.5	674.0	0.89	12.05	0.7105	0.0261	0.0884	0.0016	0.50	0.0610	0.0016	546	10	545	15	633	55	100	86
12.1	1067.1	2176.9	0.49	5.79	0.6211	0.0220	0.0796	0.0014	0.51	0.0572	0.0014	494	9	491	14	494	52	101	100
13.1	2020.0	3068.7	0.66	0.63	0.7034	0.0233	0.0878	0.0015	0.53	0.0590	0.0013	543	9	541	14	562	47	100	97
14.1	297.8	885.5	0.34	2.07	0.7617	0.0256	0.0917	0.0017	0.55	0.0602	0.0013	566	10	575	15	604	47	98	94
15.1	364.0	1073.3	0.34	5.40	0.6142	0.0210	0.0757	0.0015	0.58	0.0585	0.0013	470	9	486	13	541	48	97	87
16.1	276.1	1055.5	0.26	7.94	0.7599	0.0265	0.0949	0.0017	0.51	0.0589	0.0014	585	10	574	15	556	52	102	105
17.1	2120.1	3117.6	0.68	4.86	0.6906	0.0228	0.0854	0.0015	0.54	0.0598	0.0013	529	9	533	14	590	47	99	90
17.2	65.0	140.4	0.46	0.77	7.8500	0.2962	0.4191	0.0102	0.65	0.1404	0.0031	2256	46	2214	33	626	38	102	101
18.1	203.3	561.2	0.36	1.47	0.5634	0.0196	0.0666	0.0013	0.55	0.0610	0.0014	416	8	454	13	626	49	92	66
19.1	1935.6	3007.0	0.64	3.99	0.7391	0.0240	0.0901	0.0016	0.54	0.0597	0.0013	556	9	562	0.014	586	46	99	95
20.1	158.6	180.3	0.88	6.56	0.8627	0.0285	0.0991	0.0018	0.55	0.0621	0.0014	609	11	632	0.015	626	48	96	91
21.1	1216.2	2842.8	0.43	3.50	0.6917	0.0231	0.0823	0.0016	0.57	0.0614	0.0013	510	9	534	0.014	626	46	95	79
21.2	1258.6	2885.3	0.44	3.62	0.7259	0.0238	0.0857	0.0015	0.54	0.0617	0.0013	530	9	554	0.014	626	46	96	80
22.1	662.0	1841.3	0.36	0.80	0.7443	0.0100	0.0923	0.0006	0.45	0.0594	0.0005	569	3	565	0.006	575	20	101	99
23.1	249.9	1372.6	0.18	1.82	0.7396	0.0101	0.0898	0.0006	0.49	0.0594	0.0004	555	4	562	0.006	576	16	99	96
24.1	1785.9	2937.6	0.61	7.19	0.6985	0.0101	0.0866	0.0007	0.56	0.0585	0.0004	536	4	538	0.006	541	16	100	99
25.1	1964.1	3249.3	0.60	7.33	0.7348	0.0121	0.0913	0.0012	0.78	0.0593	0.0004	563	7	559	0.007	572	15	101	98
26.1	275.8	1087.3	0.25	0.38	0.7434	0.0101	0.0895	0.0006	0.47	0.0605	0.0004	553	3	564	0.006	626	16	98	90
27.1	128.5	448.0	0.29	0.27	0.7911	0.0141	0.0955	0.0006	0.37	0.0601	0.0008	588	0.004	592	0.008	626	0.029	99	98
28.1	156.8	221.8	0.71	1.38	0.8034	0.0114	0.0942	0.0007	0.56	0.0608	0.0005	581	0.004	599	0.006	626	0.018	97	93
29.1	528.7	556.7	0.95	10.44	0.7327	0.0123	0.0896	0.0009	0.59	0.0590	0.0007	553	0.005	558	0.007	562	0.024	99	98
30.1	1379.6	2743.9	0.50	7.78	0.6835	0.0088	0.0828	0.0005	0.48	0.0605	0.0004	513	0.003	529	0.005	626	0.016	97	83
31.1	2267.0	4019.2	0.56	9.73	0.7588	0.0113	0.0932	0.0009	0.65	0.0602	0.0004	575	0.005	573	0.006	605	0.015	100	95

Table 1 (continued)

Spot	Contents (µg/g) %				Isotopic ratios							Isotopic ages (Ma)						Conc %	
	Th	U	Th/U	C Pb	$^{207}Pb/^{235}U$	1σ	$^{206}Pb/^{238}U$	1σ	ρ	$^{207}Pb/^{206}Pb$	1σ	$T_{206/238}$	1σ	$T_{207/235}$	1σ	$T_{207/206}$	1σ	1	2
32.1	29.8	74.3	0.40	1.51	4.2350	0.0616	0.2664	0.0020	0.52	0.1180	0.0008	1522	0.010	1681	0.012	626	0.012	91	79
32.2	212.3	884.6	0.24	3.05	0.7119	0.0142	0.0878	0.0007	0.37	0.0600	0.0010	543	0.004	546	0.008	597	0.034	99	91
33.1	630.1	1324.9	0.48	2.83	0.7485	0.0151	0.0905	0.0008	0.47	0.0600	0.0013	559	0.005	567	0.009	598	0.045	98	93

C Pb common Pb, % *Conc 1* concordance calculated as ($^{206}Pb–^{238}U$ age/$^{207}Pb–^{235}Pb$ age) × 100, % *Conc 2* concordance calculated as ($^{206}Pb–^{238}U$ age/$^{207}Pb–^{206}Pb$ age) × 100

334 ppm) and U (50–363 ppm) contents and a reasonably wide range in Th/U ratios (0.11–1.21); (2) low CL intensity crystals (grains 2, 10, 13, 14, 17, 18, 19 and 20—Fig. 10c) with a relatively wide range in Th (108–1590 ppm) and U (526–1136 ppm) contents and a reasonably wide range in Th/U ratios (0.15–1.40); (3) darker rims (spots 4.1, 5.1, 9.1, 11.1, 15.2) with a relatively wide range in Th (11–657 ppm) content, narrow range in U (357–841 ppm) content, and a wide range in Th/U ratios (0.08–1.20) (Table 3).

The crystallization age of the quartz microdiorite is recorded in autocrysts (spots 13.1, 15.2, 18.1, 19.1, 20.1—Fig. 10c) at 623.7 ± 2.3 Ma (Fig. 11d). Ages of 655 Ma (spots 4.1, 5.1, 10.1—Fig. 10c) are recorded in darker rims and mantle of possibly antecrysts and may be interpreted as a result of the hypothetical first magma pulse. An older age of 680 Ma (spots 2.1, 9.1—Fig. 10c) is recorded in darker rim of inherited cores.

Paleoproterozoic and Mesoproterozoic ages (Fig. 11d) are recorded both in xenocrysts (zircon crystals 1, 3, 7, 8, 12, 16—Fig. 10c) or inherited core (zircon 15—Fig. 10c).

Lu–Hf analysis of zircon

All Lu–Hf analyses were carried out by LA-ICP-MS at points as close as possible of U–Pb spot analyses always in the same CL sector of the zircon crystal (Fig. 10a) making more robust the correlation of εHf and Hf T_{DM} values at the time of crystallization (Fig. 12a). Zircon Hf T_{DM} model ages are usually referred to as crust formation ages (Hawkesworth and Kemp 2006). The Lu–Hf isotope compositions for 11 grains from sample 1 (K-54A) are summarized in Table 4. Typically, average $^{176}Lu/^{177}Hf$ ratios are very low, ranging from 0.000498 to 0.002009.

Zircon crystals from K-54A monzogranite show mean values of the $^{176}Hf/^{177}Hf(t)$ isotopic composition ranging from 0.281899 to 0.282020, that corresponds to a total variation of about five ε-units [εHf(t) = − 17.26 to − 12.51].

An average of Hf T_{DM} model ages of 2.38 Ga, and εHf(t) values around − 14.7 were acquired on zircons of ages of the last period of the magmatic pulse of the pluton (group 2.3–2.4 Ga, Fig. 12a). Exception of zircon 19.1 with older Hf T_{DM} model age (2.5 Ga) and more εHf(t) negative value (− 17.02), values were very similar to zircon 6.1 (Fig. 10a) of 618 Ma (group 2.5–2.6 Ga, Fig. 12a). One spot representing older age (705 Ma) provide considerably less negative εHf(t) of − 4.56 and much younger Hf T_{DM} model ages of 1.86 Ga (Fig. 12a). In broad spectrum, an overall decrease in εHf from the oldest to the youngest magmatic pulse is observed (Fig. 12b).

The negative εHf(t) values suggest derivation from a source with much lower Lu/Hf ratio than the chondritic reservoir, i.e., the sources of zircon crystals for the monzogranite have clearly crustal affinities. The igneous protolith

Table 2 Results of U–Pb LA-ICP-MS dating of zircons on biotite monzogranite of ROP—sample 2 (K-190A)

Spot	Contents (µg/g) %				Isotopic ratios							Isotopic ages (Ma)						Conc %	
	Th	U	Th/U	C Pb	$^{207}Pb/^{235}U$	1σ	$^{206}Pb/^{238}U$	1σ	ρ	$^{207}Pb/^{206}Pb$	1σ	$T_{206/238}$	1σ	$T_{207/235}$	1σ	$T_{207/206}$	1σ	1	2
1.1	604.8	644.8	0.94	0.61	0.9305	0.0239	0.1123	0.0009	0.98	0.0601	0.0016	686	5	668	13	607	58	102	113
1.2	50.2	414.4	0.12	1.83	0.8684	0.0479	0.1059	0.0013	0.85	0.0595	0.0037	649	8	635	26	584	127	102	111
2.1	120.8	292.7	0.41	0.44	0.8191	0.0252	0.0970	0.0009	0.58	0.0613	0.0020	597	5	608	14	649	70	98	91
3.1	24.1	69.7	0.35	1.69	0.7656	0.1316	0.0994	0.0030	0.15	0.0559	0.0099	611	18	577	81	447	305	105	136
4.1	57.8	141.3	0.41	0.78	0.8675	0.0422	0.1019	0.0012	0.65	0.0618	0.0032	625	7	634	23	666	113	98	93
5.1	96.7	270.5	0.36	0.77	0.8426	0.0338	0.1026	0.0011	0.79	0.0596	0.0026	630	6	621	19	587	94	101	107
6.1	56.4	157.9	0.36	0.48	1.1695	0.0369	0.1300	0.0012	0.80	0.0652	0.0021	788	7	786	17	782	68	100	100
7.1	54.3	96.2	0.57	0.66	0.8349	0.0583	0.1007	0.0015	0.39	0.0601	0.0045	618	9	616	32	609	160	100	101
8.1	67.3	556.3	0.12	1.12	0.8393	0.0198	0.1016	0.0008	0.78	0.0599	0.0014	624	5	619	11	601	51	100	103
9.1	96.2	789.9	0.12	1.42	0.9308	0.0195	0.1128	0.0008	0.97	0.0598	0.0013	689	5	668	10	598	46	103	115
10.1	98.1	318.4	0.31	1.12	0.9572	0.0326	0.1125	0.0011	0.93	0.0617	0.0022	687	6	682	17	664	75	100	103
11.1	115.6	92.5	1.25	0.24	0.8165	0.0470	0.0998	0.0013	0.43	0.0593	0.0037	613	8	606	26	580	133	101	105
12.1	9.2	589.5	0.02	0.15	0.8839	0.0185	0.1053	0.0009	0.91	0.0609	0.0014	646	6	643	10	634	50	100	101
13.1	75.2	86.4	0.87	5.46	0.8004	0.0755	0.0979	0.0023	0.84	0.0593	0.0062	602	14	597	42	578	222	100	104
14.1	62.9	616.7	0.10	1.02	0.9739	0.0250	0.1171	0.0012	0.68	0.0603	0.0017	714	7	691	13	614	62	103	116
15.1	31.5	58.7	0.54	4.72	0.9214	0.0936	0.1076	0.0028	0.61	0.0621	0.0074	659	16	663	49	678	275	99	97
16.1	59.7	48.0	1.24	4.52	0.8825	0.1098	0.1029	0.0032	0.35	0.0622	0.0089	632	19	642	58	681	310	98	92
17.1	126.8	636.8	0.20	1.66	0.8562	0.0197	0.1033	0.0010	0.97	0.0601	0.0015	634	6	628	11	607	58	100	104
18.1	75.5	662.3	0.11	0.28	0.9073	0.0216	0.1101	0.0011	0.55	0.0597	0.0015	674	6	656	12	594	57	102	113
19.1	42.8	156.7	0.27	1.31	0.7899	0.0394	0.0974	0.0014	0.77	0.0588	0.0034	599	8	591	22	560	119	101	106
20.1	109.7	477.9	0.23	0.81	0.8107	0.0194	0.0992	0.0010	0.98	0.0593	0.0015	610	6	603	11	577	53	101	105
21.1	87.2	414.2	0.21	0.91	0.8198	0.0228	0.0988	0.0010	0.91	0.0602	0.0018	608	6	608	13	610	65	99	99
22.1	176.9	620.5	0.29	0.18	0.8810	0.0189	0.1042	0.0010	0.55	0.0613	0.0014	639	6	642	10	651	51	99	98
23.1	205.4	290.8	0.71	0.11	6.2845	0.1045	0.3491	0.0031	0.56	0.1306	0.0023	1931	15	2016	14	2105	31	95	91

C Pb common Pb, *% Conc 1* concordance calculated as (^{206}Pb–^{238}U age/^{207}Pb–^{235}Pb age) × 100, *% Conc 2* concordance calculated as (^{206}Pb–^{238}U age/^{207}Pb–^{206}Pb age) × 100

Table 3 Results of U–Pb LA-ICP-MS dating of zircons on quartz microdiorite of ROP—sample 3 (K-190B)

Spot	Contents (μg/g) %				Isotopic ratios							Isotopic ages (Ma)						Conc. %	
	Th	U	Th/U	C Pb	$^{207}Pb/^{235}U$	1σ	$^{207}Pb/^{235}U$	1σ	ρ	$^{207}Pb/^{206}Pb$	1σ	$T_{206/238}$	1σ	$T_{207/235}$	1σ	$T_{207/206}$	1σ	1	2
1.1	121.2	362.9	0.33	0.35	6.0283	0.0917	0.3503	0.0029	0.94	0.1248	0.0021	1936	14	1980	13	2026	29	97	95
2.1	268.8	903.1	0.30	1.19	0.9219	0.0203	0.1126	0.0010	0.91	0.0594	0.0015	688	6	663	11	582	55	103	118
3.1	28.0	151.4	0.19	0.98	5.3196	0.0857	0.3165	0.0027	0.01	0.1219	0.0022	1773	14	1872	14	1984	33	94	89
3.2	16.1	102.6	0.16	0.07	6.1363	0.1059	0.3714	0.0032	0.89	0.1198	0.0022	2036	15	1995	14	1954	32	102	104
4.1	656.8	552.2	1.19	0.67	0.8831	0.0291	0.1064	0.0013	0.97	0.0602	0.0022	652	8	643	16	611	78	101	106
5.1	65.0	804.3	0.08	0.43	0.8789	0.0184	0.1062	0.0010	0.71	0.0600	0.0014	650	6	640	10	605	51	101	107
6.1	66.1	156.6	0.42	0.08	4.6502	0.0890	0.3060	0.0031	0.81	0.1102	0.0025	1721	15	1758	16	1803	41	97	95
6.2	333.9	276.5	1.21	8.47	1.2737	0.0415	0.1251	0.0016	0.8	0.0739	0.0028	760	9	834	19	1038	77	91	73
7.1	39.0	357.5	0.11	0.07	6.1576	0.0935	0.3571	0.0029	0.16	0.1250	0.0021	1969	14	1999	13	2030	29	98	96
8.1	175.9	280.0	0.63	0.03	4.6876	0.0775	0.3111	0.0027	0.94	0.1093	0.0021	1746	13	1765	14	1788	35	98	97
8.2	17.8	50.2	0.35	0.76	4.8345	0.1601	0.3120	0.0054	0.18	0.1124	0.0045	1751	26	1791	28	1838	75	97	95
9.1	241.3	840.9	0.29	0.22	0.9255	0.0183	0.1117	0.0010	0.93	0.0601	0.0013	683	6	665	10	607	48	102	112
10.1	1589.3	1135.5	1.40	1.02	0.8955	0.0171	0.1081	0.0009	0.97	0.0601	0.0012	662	5	649	9	606	44	101	109
11.1	75.2	786.9	0.10	1.41	1.0066	0.0224	0.1199	0.0011	0.95	0.0609	0.0014	730	7	707	11	635	51	103	115
12.1	20.6	56.7	0.36	0.89	4.8821	0.1458	0.3208	0.0049	0.56	0.1104	0.0040	1794	24	1799	25	1806	63	99	99
13.1	681.8	558.9	1.22	0.20	0.8339	0.0191	0.1015	0.0010	0.82	0.0596	0.0015	623	6	616	11	588	55	101	105
14.1	339.9	507.9	0.67	0.69	0.8431	0.0219	0.1035	0.0011	0.91	0.0591	0.0017	635	6	621	12	570	62	102	111
15.1	10.9	356.9	0.03	0.14	6.1028	0.0884	0.3523	0.0026	0.66	0.1256	0.0020	1946	13	1991	13	2038	28	97	95
15.2	210.7	976.3	0.22	0.13	0.8366	0.0155	0.1010	0.0008	0.76	0.0601	0.0012	620	5	617	9	606	43	100	102
16.1	72.9	134.5	0.54	0.11	5.3402	0.1055	0.3527	0.0036	0.93	0.1098	0.0025	1947	17	1875	17	1797	41	103	108
17.1	107.7	723.9	0.15	0.72	0.5994	0.0148	0.0723	0.0007	0.96	0.0601	0.0016	450	4	477	9	608	60	94	74
18.1	348.8	639.9	0.55	0.65	0.8320	0.0191	0.1005	0.0010	0.94	0.0601	0.0015	617	6	615	11	606	54	100	101
19.1	225.0	525.6	0.43	0.36	0.8472	0.0202	0.1015	0.0010	0.01	0.0605	0.0016	623	6	623	11	622	57	100	100
20.1	251.6	628.7	0.40	1.20	0.8408	0.0190	0.1022	0.0010	0.83	0.0596	0.0015	628	6	620	11	591	54	101	106

C Pb common Pb, % *Conc 1* concordance calculated as (^{206}Pb–^{238}U age/^{207}Pb–^{235}Pb age) × 100, % *Conc 2* concordance calculated as (^{206}Pb–^{238}U age/^{207}Pb–^{206}Pb age) × 100

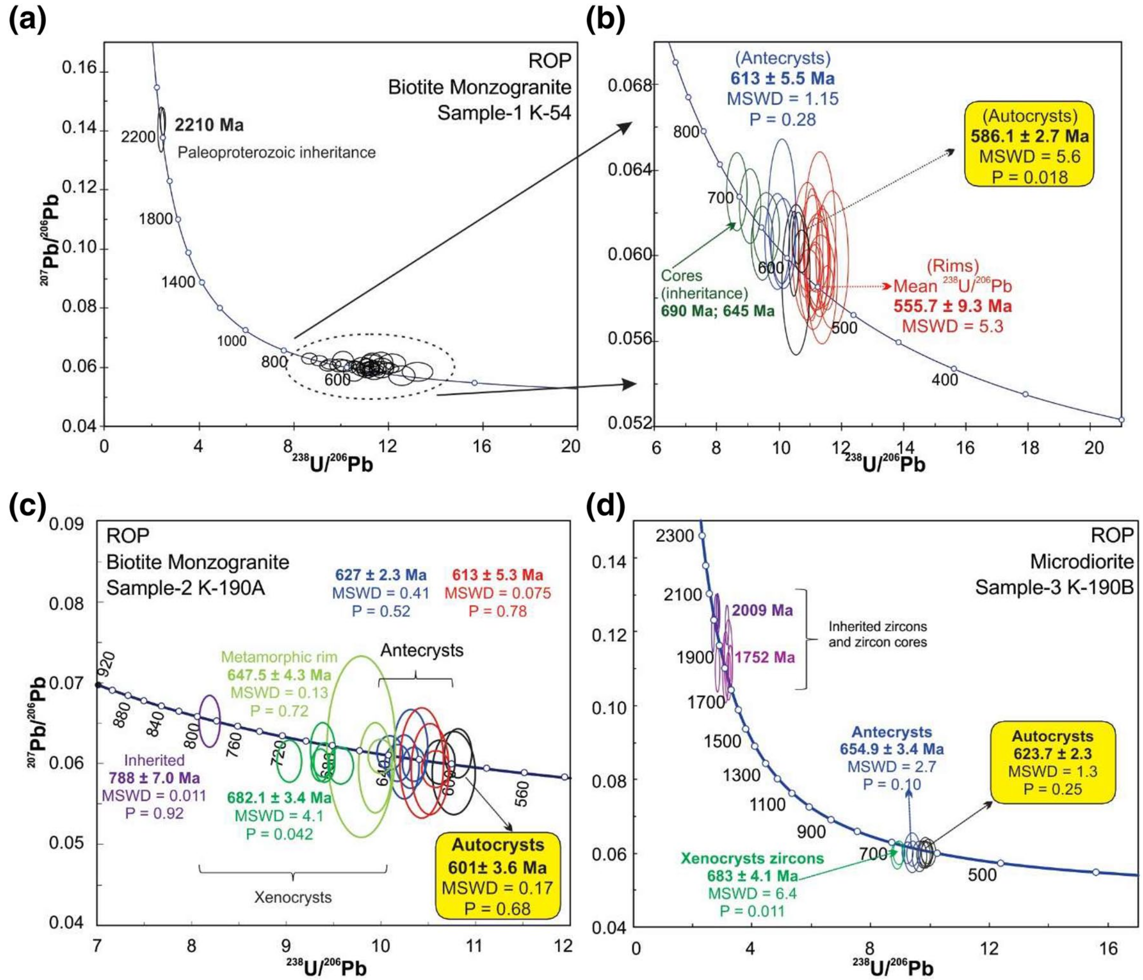

Fig. 11 LA-ICP-MS zircon U–Pb concordia diagram for the ROP. All given ages are Concordia ages or, when specified, mean $^{238}U/^{206}Pb$ ages. *P* probability of concordance. Paleoproterozoic inheritances are given in mean $^{238}U/^{206}Pb$ ages. The **a** U–Pb plot of zircon crystals from the ROP monzogranite—sample 1 (K-54A). **b** Detail of Neoproterozoic zircon crystals from the ROP monzogranite—sample 1 (K-54A) (see text for explanation). **c** U–Pb plot of zircon crystals from the ROP monzogranite—sample 2 (K-190A) (see text for explanation). Data-point error ellipses are 2σ. **d** U–Pb plot of zircon crystals from the ROP quartz microdiorite—sample 3 (K-190B) (see text for explanation)

of this granite probably were added to the continental crust in Siderian times as indicated by the zircon Hf model ages.

Trace elements in zircon

The result of the trace-element analysis is given in Table 5. 12 spots in 9 investigated zircon crystals from sample K-54A of the ROP monzogranite were analysed. For the calibration procedure, two glass standards NIST610 were used. After each group of six scan lines (rasters-R), a quality control analysis of the zircon standard ZR 91500 was made, and to finalize the analyses of each sample, a single analysis of the glass standard NIST 612 and two more analyses of the NIST 610 standard were made (Table 5). The following images were made of analysed zircons from sample 1 (location on Fig. 3) showing the spots of the raster lines (Fig. 13). The spot diameter was 25 µm. The other spots are the sites of analyses of U–Pb and Hf.

Zircons from the monzogranite have relatively high Th/U ratios (0.24–1.07—Table 1) indicating a magmatic origin (Rubatto 2002; Hoskin and Schaltegger 2003). Just one Th/U ratio of 0.08 was observed in the raster 6 of the zircon-8 rim (Zr-8—Fig. 13c; Table 5). The zircon crystals have high concentrations of Th and U (Table 5), generally varying from 240 ppm to 820 ppm and 600 ppm to 2200 ppm, respectively. An exception is two analyses, the zircon-7 rim with 6615 ppm of Th and 7354 ppm of U and zircon-8 with 60 ppm of Th.

Hafnium shows concentrations varying within the range of 1.3–2.0 wt%. Y exhibits high concentrations in analysed zircons varying between 800 and 5400 ppm. The Nb/Ta ratios vary from 2 to 8 and the highest value is found in the

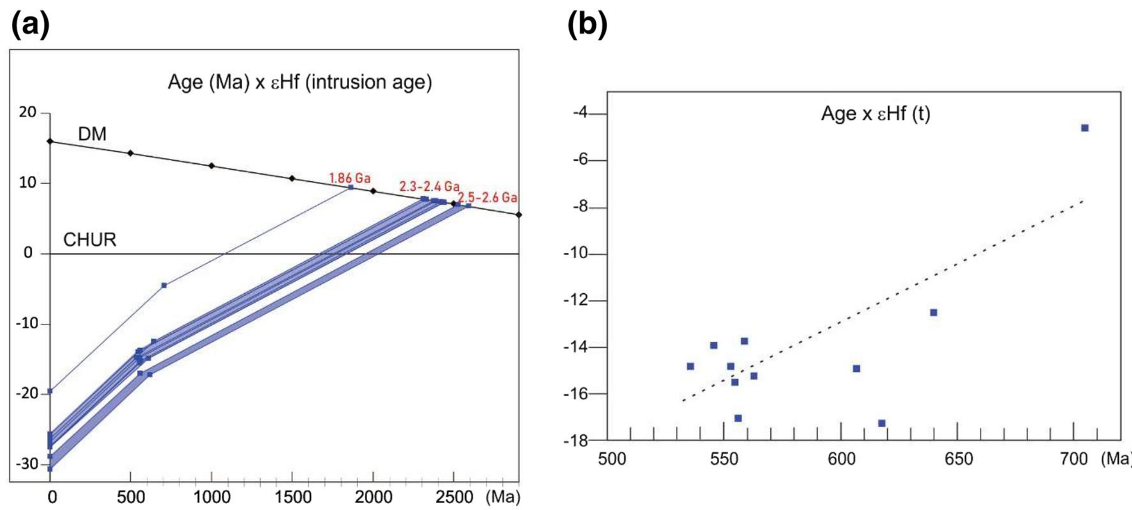

Fig. 12 Hf isotope composition of zircon crystals from the ROP monzogranite (sample 1, K-54A): **a** εHf(*t*) versus intrusion age diagram. The evolution trends were calculated for a $^{176}Lu/^{177}Hf$ of 0.0113. *DM* depleted mantle evolution line, *CHUR* chondritic uniform reservoir. **b** Plot of $^{206}Pb/^{238}U$ zircon ages versus εHf(*t*)

youngest zircon (Zr 7-spot 7.2—518 Ma, Fig. 10a) that is enriched in all REE comparative with other zircons.

The REE geochemistry of zircons and its chondrite-normalized REE patterns show depleted light REE and enriched heavy REE, some positive Ce, and weak negative Eu anomalies, although some zircons did not show Eu anomaly (Table 5; Fig. 14a). The REE patterns show that the incorporation of most REE correlates with younger zircons and possibly with a hydrothermal event.

The data obtained of ratios of REE concentrations in the zircon crystals versus the REE content in the host rock (sample 1, K-54A) show that the HREEs are strongly concentrated by the zircons, with high partition coefficients, varying from 100 to 3000 (Table 6, Fig. 14b). The LREEs, however, have much lower coefficients, mostly in the range of 1–20. U and Y are preferred in the zircon structure in relation to Th, Ta, and Nb, which is reflected in their higher partition coefficients (Table 6). Ta is preferred in relation to Nb, typical from non-A-type granites (Table 6).

In $(Sm/La)_N$ vs. La (Fig. 14c) and Ce/Ce* vs. $(Sm/La)_N$ (Fig. 14d), diagrams widely used to discriminate magmatic from hydrothermal zircons, most zircons analysed plot close to the “hydrothermal” field defined by Hoskin (2005), or even into others hydrothermal fields compiled from several magmatic and hydrothermal zircons by Zhong et al. (2018).

In a broad sense, a positive correlation between zircon Th/U and Ti-in zircon temperature and between Th/U and Zr/Hf is observed (Fig. 15a–c). This indicates that higher temperature crystallization in less fractionated magmas is associated with elevated zircon Th/U ratios. Also, the positive correlation between Ti-in-zircon temperature and zircon Th/U (Fig. 15a) and $(Th_{(zircon/rock)}/U_{(zircon/rock)})$ (Fig. 15c) suggest that cooler more fractionated melts containing more U in the zircon crystals, due to the less-incompatible nature of U in relation to Th (e.g., Kirkland et al. 2015). The raster 3 of Zr-7 (Fig. 13b) that represents probably an age of ca. 518 Ma (spot 7.2—Fig. 10a) is usually out of the trends.

Discussion

Finely foliated biotite monzogranite and quartz microdiorite compose the ROP of the MC-CoT. Magma mingling features is observed by field evidence (Figs. 3, 6) and petrographic analyses (Figs. 4, 5). Physical accumulation of K-feldspar megacrysts in clusters with no evident boundary, highlighting the occurrence of instabilities that change considerably these mineral proportions are also supported by petrographic studies. The physical accumulation by mingling of K-feldspar megacrysts resulted in concentrations in irregular patches and dike-like bodies with diffuse boundaries (Figs. 3a, b, 6) are also found as suggested by Paterson et al. (2005).

Magmatic flow in ROP is mainly represented by alignment and imbrication of undeformed euhedral K-Feldspar crystals and elongation of microdiorite enclaves consistent with rotation of crystals in a melt phase (Vernon 2000). On the other hand, evidences of solid-state flow are found, possible under influence of the high-angle ductile shear zones that limit the MC. Folded foliation, quartz dynamic recrystallization, recrystallization of plagioclase, and shear bands are typical microstructures in microdiorite, and a foliation expressed by segregated bands of quartz and aligned biotite crystals and K-feldspar recrystallization is

Table 4 Results of Lu–Hf LA-MC-ICP-MS data of zircons on biotite monzogranite of ROP—sample 1 (K-54A)

Grain/spot	$^{176}Hf/^{177}Hf$	± 2 SE	$^{176}Lu/^{177}Hf$	± 2 SE	U–Pb age (*T*1) Ma	εHf(0)	$^{176}Hf/^{177}Hf$ (*T*1)	εHf (*T*1)	$^{176}Hf/^{177}Hf_{DM}(T)$	T_{DM} (Ma)	$^{176}Hf/^{177}Hf_{DM}(T)$	εHf (T_{DM})
4.1	0.281995	0.000037	0.002009	0.0000345	607	−27.47	0.281972	−14.92	0.282786	2438	0.281432	7.33
6.1	0.281906	0.000053	0.000590	0.0000097	618	−30.62	0.281899	−17.26	0.282778	2593	0.281315	6.76
7.2	0.282028	0.000036	0.000652	0.0000116	640	−26.32	0.282020	−12.51	0.282762	2313	0.281526	7.79
9.1	0.282218	0.000030	0.001113	0.0000277	705	−19.59	0.282203	−4.56	0.282715	1863	0.281862	9.43
10.1	0.281996	0.000050	0.000717	0.0000043	555	−27.46	0.281988	−15.51	0.282824	2435	0.281435	7.34
11.1	0.282047	0.000058	0.000719	0.0000037	546	−25.65	0.282039	−13.89	0.282830	2327	0.281516	7.74
19.1	0.281956	0.000026	0.001093	0.0000102	556	−28.84	0.281945	−17.02	0.282823	2529	0.281363	7.00
24.1	0.282027	0.000058	0.000627	0.0000074	536	−26.36	0.282020	−14.79	0.282838	2375	0.281479	7.56
25.1	0.281997	0.000021	0.000498	0.0000032	563	−27.41	0.281992	−15.21	0.282818	2422	0.281444	7.39
29.1	0.282015	0.000062	0.000598	0.0000132	553	−26.78	0.282008	−14.83	0.282825	2391	0.281468	7.50
33.1	0.282046	0.000043	0.001027	0.0000275	559	−25.66	0.282036	−13.74	0.282821	2327	0.281515	7.74

The spot number is the same as the U–Pb analysis

observed in monzogranites. Additionally, microstructures in ROP monzogranite indicate fracturing of K-feldspar crystals in the presence of melt (Fig. 4c). As postulated by Bouchez et al. (1992), fracturing resulted from concentration of stress at contacts between grains when the granite contains submagmatic nature. The presence of a submagmatic flow in monzogranites suggests that the crystallization of this pluton undergone to some strain. Conversely, the grain flow is not observed in quartz microdiorite. The implications for the observed deformations and the emplacement chronology of the two bodies are discussed in the following item.

The irregular elongate and flame-like shape enclave swarms indicate the relative flow direction between the acid and intermediate magmas (Fig. 3a, b), suggesting that both acid and the intermediate magmas were melted during flow.

In a polycyclic terrane where reworking of the continental crust is evident (Table 7), the high-precision U–Pb zircon dating provides significant U–Pb age range (556–613 Ma and 601–627 Ma on monzogranite and 624–655 Ma on quartz microdiorite, Fig. 11), reflecting prolonged timescales of zircon crystallization and long magma residence times. According to Samperton et al. (2017), such age heterogeneity may indicate prolonged crystallization between the temperatures of zircon saturation and rock solidification, stressing the condition of considering zircon as a zoned, dynamic archive.

The discrimination of autocryst, antecryst, and xenocryst in terranes with complex crustal histories is a hard work, but the CL images analyses allow us make some interpretations. Nevertheless, as pointed out by Miller et al. (2007), the line between xenocryst and antecryst could be indistinct. Table 7 presents a resume of some available ages of IS and Areado pluton of the MC along with the ages reported in this work, which discriminate the origin of zircon crystals.

A late-stage magmatic episode of the ROP monzogranite of 556 Ma is given by spots in darker rims with sector zoning, although several pulses of zircon crystallization are recorded through several time spam, i.e., 627 Ma; 613 Ma, 601 Ma, and 586 Ma. The initial crystallization of the older intermediate material is constrained at ca. 655 Ma and the final crystallization age around 624 Ma.

In contrast to usual magmatic zircon, the weak CL (apart from inherited zircon cores or xenocrysts), the enrichment of REE in darker rims (Zr 32-R1; Zr 7-R3; Zr8-R5; Zr12-R9; Figs. 13, 14a), the distribution on $(Sm/La)_N$ vs. La and Ce/Ce* vs. $(Sm/La)_N$ diagrams (Fig. 14c, d), and variable Th/U ratios suggest that the ROP analysed zircons may contain domains of hydrothermal origin (Hoskin 2005; Harley et al. 2007; Wang et al. 2016; Zhong et al. 2018). Nevertheless, more detailed zircon geochemistry to differentiate magmatic and hydrothermal zircons is necessary to make this interpretation unequivocal.

Table 5 Trace element and REE (ppm) data ($\pm 1\sigma$) for zircon crystals from the ROP biotite monzogranite—sample 1 (K-54A)

Element	ZR 32				ZR 7				ZR 8				ZR 9		ZR 33		ZR 12		ZR 23		ZR 26		ZR 21		ZR standard	
	R1	1σ	R2	1σ	R3	1σ	R4	1σ	R5	1σ	R6	1σ	R7	1σ	R8	1σ	R9	1σ	R10	1σ	R11	1σ	R12	1σ	zr 91500	1σ
Li	12.5	1.1	6.2	0.7	150.3	7.3	21.9	1.7	42.8	3.4	24.1	2.3	1.3	0.7	11.1	1.8	38.0	3.4	52.4	3.1	35.2	2.5	30.9	2.6	3.18	0.22
Mg	11.3	1.1	2.6	0.5	46.5	3.1	5.0	0.8	16.6	2.2	271.1	17.3	13.1	1.5	83.2	6.8	39.4	4.0	35.6	2.7	167.1	12.4	63.0	5.4	0.91	0.11
Al	445.0	16.1	74.2	3.2	1809.9	63.1	379.7	14.3	229.2	10.4	1667.7	60.4	290.8	11.7	335.8	14.4	380.6	16.4	366.5	13.9	601.0	23.1	203.9	9.1	17.39	0.71
P	310.4	87.7	366.2	100.7	1673.7	449.6	374.2	106.7	113.8	51.1	741.1	211.4	996.0	292.2	170.1	68.3	110.4	58.0	109.7	38.5	175.5	60.8	79.7	38.5	28.52	8.89
Ti	65.0	5.8	31.0	3.2	219.7	12.6	37.1	4.9	28.8	6.6	71.3	9.4	20.4	4.0	209.3	18.1	140.7	15.3	87.1	5.8	48.2	5.4	24.0	4.7	6.02	0.59
Rb	< 0.49	0.2	< 0.38	0.2	0.7	0.3	0.5	0.3	< 0.35	0.3	5.1	0.9	1.7	0.5	0.9	0.5	0.7	0.6	< 0.31	0.2	< 0.36	0.3	0.8	0.4	< 0.070	0.032
Sr	3.2	0.4	0.9	0.2	31.5	2.0	1.2	0.3	4.2	0.7	1.9	0.4	1.8	0.3	3.7	0.7	7.3	1.0	7.1	0.6	12.8	1.1	5.0	0.7	0.19	0.029
Y	1599.4	74.8	1554.1	73.4	5400.8	258.3	1293.5	63.2	715.8	36.4	825.1	42.5	3663.3	199.8	1982.7	111.6	1000.1	58.3	799.4	47.4	1785.6	108.9	649.3	41.1	155.12	8.06
Nb	15.2	0.9	9.7	0.6	91.2	3.6	10.3	0.7	8.4	0.9	1.9	0.4	6.4	0.6	12.5	1.1	8.8	1.0	7.7	0.5	20.9	1.2	6.8	0.7	1.099	0.072
Ba	4.3	1.1	< 0.39	0.3	26.2	2.9	1.9	0.8	1.2	1.0	15.0	3.2	2.6	1.1	1.4	1.2	2.8	1.5	2.3	0.6	1.4	0.7	2.3	1.1	< 0.141	0.044
La	69.7	3.0	7.3	0.5	160.1	6.6	31.8	1.7	26.2	1.9	7.5	0.8	13.2	1.0	14.5	1.3	54.6	3.3	43.0	2.1	27.1	1.6	17.4	1.3	0.0061	0.0043
Ce	313.9	13.1	63.2	2.8	796.3	33.3	167.8	7.5	148.1	7.3	44.6	2.6	62.4	3.3	115.8	6.3	384.3	19.5	274.4	13.8	242.7	12.7	64.1	3.8	3.27	0.18
Pr	48.5	2.0	6.6	0.4	109.0	4.3	21.4	1.1	19.1	1.4	6.0	0.6	10.9	0.8	13.0	1.1	39.5	2.3	43.5	1.9	29.7	1.5	10.4	0.8	0.0223	0.0081
Nd	332.2	23.7	46.3	4.0	640.1	46.0	161.6	13.3	113.5	11.8	40.9	5.5	81.7	8.5	112.8	12.6	231.8	24.1	316.0	29.9	232.8	23.6	68.6	8.5	0.09	0.059
Sm	170.2	9.3	31.3	2.3	359.7	18.4	99.5	6.6	50.7	5.6	20.0	3.1	55.7	4.8	66.1	6.6	131.7	11.1	157.9	9.8	124.2	8.8	45.8	4.7	0.43	0.091
Eu	40.7	2.0	7.3	0.6	87.7	3.8	24.0	1.5	17.2	1.8	6.4	0.9	14.2	1.2	16.7	1.7	39.2	3.0	46.1	2.2	27.7	1.7	6.8	0.9	0.232	0.039
Gd	175.1	7.5	57.8	3.0	436.2	16.2	125.0	6.3	55.7	5.2	26.1	3.2	142.0	7.4	117.1	7.9	143.7	9.5	155.3	6.4	140.1	6.9	48.0	3.9	2.49	0.21
Tb	27.4	1.4	15.8	0.9	85.2	4.0	19.0	1.2	10.3	1.0	6.1	0.7	37.2	2.2	23.3	1.7	21.0	1.7	20.5	1.2	24.3	1.6	8.5	0.8	1.001	0.069
Dy	191.4	9.7	156.6	7.8	660.7	31.2	154.5	8.7	76.3	6.5	67.7	5.7	414.1	23.0	224.1	14.7	109.1	8.9	106.9	6.5	207.9	13.1	63.1	5.3	12.68	0.74
Ho	54.3	2.7	53.0	2.6	193.2	9.2	44.6	2.4	23.3	1.7	27.2	1.8	130.0	7.2	71.9	4.4	30.9	2.3	25.7	1.6	62.9	3.9	20.5	1.6	5.26	0.29
Er	221.1	9.3	214.9	8.9	772.8	31.2	179.0	8.1	100.9	6.1	144.3	7.7	550.7	25.0	292.1	14.8	113.0	7.1	99.0	5.0	280.4	14.0	95.5	5.8	28.19	1.25
Tm	43.2	2.1	43.7	2.1	141.9	6.6	38.7	2.0	22.4	1.6	40.4	2.4	108.9	5.8	57.4	3.5	23.8	1.8	20.6	1.2	56.4	3.4	19.6	1.4	7.3	0.37
Yb	443.7	23.2	402.8	21.0	1255.6	64.8	355.3	20.0	251.0	16.8	460.8	27.8	962.9	57.6	531.8	34.8	235.8	17.7	215.8	14.2	515.9	34.7	207.5	15.7	83.11	4.7
Lu	76.6	3.5	72.2	3.3	220.1	9.9	69.6	3.4	55.7	3.2	98.4	5.1	172.2	8.8	107.6	6.0	51.0	3.3	47.6	2.6	100.9	5.7	47.8	3.0	14.83	0.72
Hf	15012.7	903.6	12873.4	786.7	18077.2	1126.0	16927.4	1078.4	19434.6	1271.3	16245.0	1091.8	13243.9	974.9	15559.8	1184.7	14095.4	1110.5	19706.3	1602.1	18088.0	1522.6	20023.8	1745.0	7550.45	521.12
Ta	2.8	0.3	1.8	0.2	11.9	0.7	3.9	0.4	3.6	0.5	0.4	0.2	2.5	0.3	2.8	0.4	2.1	0.4	3.8	0.3	4.7	0.4	3.6	0.4	0.662	0.047
Th	520.7	21.0	242.4	9.9	6615.3	268.1	354.1	14.9	418.8	18.3	60.0	3.2	444.7	20.3	681.5	31.8	594.9	28.6	620.1	29.7	816.9	40.1	278.1	14.3	32.3	1.42
U	1190.0	52.9	602.7	27.1	7353.8	333.2	1323.3	61.2	2205.6	104.1	754.6	36.7	744.2	38.5	1425.8	75.6	1473.4	80.3	2011.4	111.7	2226.5	127.2	1438.0	84.7	98.24	4.82
Th/U	0.44		0.40		0.90		0.27		0.19		0.08		0.60		0.48		0.40		0.31		0.37		0.19			
Eu/Eu*	0.72		0.52		0.68		0.66		0.99		0.85		0.49		0.58		0.87		0.90		0.64		0.44			
Ce/Ce*	1.26		2.14		1.41		1.51		1.55		1.56		1.22		1.98		1.94		1.49		2.00		1.12			

R raster and equivalent zircon crystals from Figs. 10 and 13. Trace-element data for the 91500-zircon standard are included

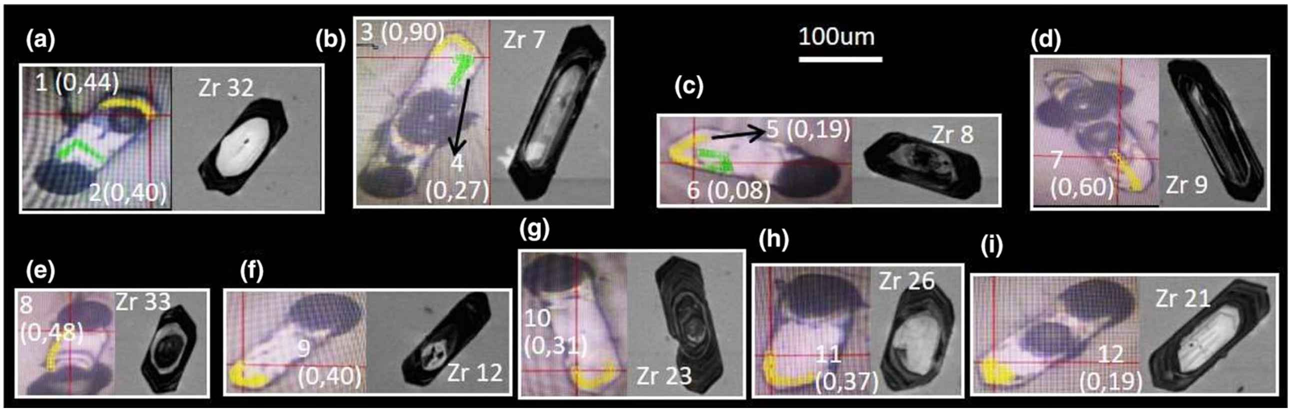

Fig. 13 Transmitted light (left) and cathodoluminescence images (right) of analysed zircon crystals—sample 1 (K-54A) by ICP-MS for trace elements. In the figure are represented the raster number with Th/U ratios values in parentheses and the zircon number (same of Fig. 10a). The green and yellow lines correspond to the rasters spots (scan lines)

Thus, the observed field relations and the older U–Pb zircon ages of the quartz microdiorite suggest that the monzogranite emplacement started probably during the medium-to-final stages of crystallization of the quartz microdiorite, and this one could react as a fluid with which the granite could mingle.

A common feature of the granites in the MC is the Paleoproterozoic and Neoproterozoic inheritances (Table 7). The Rhyacian inheritance (spots 2.2, 17.2, Fig. 10a) is quite typical in the monzogranites of the ROP and is also registered in inherited zircons of IS and in basement roof pendants in the Areado Pluton (Passarelli et al. 2016). Osirian inheritance of 2.0 Ga is found in quartz microdiorite and in monzogranite—sample 2 (spot 23.1, Fig. 10b; spots 1.1, 7.1, 15.1 and 16.1, Fig. 10c). Statherian inheritance (1.72–1.79 Ga) is only found in quartz microdiorite zircon crystals (spots 3.1, 6.1, 8.1, 8.2 and 12.1, Fig. 10c) and is not found in MC rocks (Table 7).

Ages around 790 Ma are found in xenocrysts of the ROP monzogranite and the IS rocks. On the other hand, ROP monzogranite xenocrysts of ca. 645 Ma could reflect the Itariri magmatism.

Possibly co-mingling and exchange of xenocrysts with ages between 680 and 700 Ma occurred mainly between the quartz microdiorite (spots 2.1, 9.1—Fig. 10c) and monzogranite sample 2 (spots 1.1, 9.1, 10.1, 18.1—Fig. 10b) of ROP. These xenocrysts may be incorporated from host rocks of the MC (Areado Granite and IS—Table 7).

Additionally, the difference of ages between the two samples of monzogranite may suggest that a hybrid zone was formed between the two magmas, and the sample 2, with older ages, may represent a hybrid monzogranite. The Nd and Sr isotopic data seem to corroborate this proposition.

In the conventional εNd vs. $^{87}Sr/^{86}Sr$ isotope variation diagram (Fig. 16a); along with the data for oceanic island basalts and MORB sample major reservoirs in the mantle, and data from MC rocks, no trend in the ROP data is evident. Nevertheless, the isotope data display a consistent shift away from likely oceanic isotope signatures, with lower εNd and higher $^{87}Sr/^{86}Sr$ values indicate a characteristic of the continental crust field-enriched quadrant (Fig. 16a). This behavior is in accordance with the features and ages observed in the zircons that clearly indicate the participation of the crust in its generation. Additionally, we can consider that the Sr and Nd isotope ratios for ROP rocks are distinctly less radiogenic than those of the other units of the MC.

Isotope-element mixing diagrams provide some insight into the processes and origins of Sr–Nd isotopic signatures in the ROP. These samples show a linear correlation when they are plotted in 1/Sr vs. $^{87}Sr/^{86}Sr$ and considered that the correlation observed in Rb–Sr isotope evolution diagram is probably due to two component mixing (Fig. 16b). A binary mixing array between a low-Sr concentration more radiogenic $^{87}Sr/^{86}Sr$ (~0.715) end-member (monzogranite sample 1) with a high-Sr, less radiogenic (~0.708) source (quartz microdiorite sample) probably represents a mechanical mixing (monzogranite sample 2).

In the conventional Nd isotope-element mixing diagram (Fig. 16c) the Nd data suggest also a binary mixing array between a less negative εNd, high Nd concentration source (quartz microdiorite sample) with a more negative εNd and low Nd concentration (monzogranite sample 1). Mechanical mixing probably controls the mixing array.

Moreover, the new data from the MC combined with the literature data (charnockitic rocks; Picanço 1994; Picanço et al. 1998; Pavan 2017) from the Itatins Complex (Curitiba Terrane) were plotted in Sr evolution diagram (Fig. 16d). Despite the similarity of the ROP REE pattern with those rocks originated from charnockite fusion, the ROP rocks are plotted below the evolution lines of the Itatins Complex charnockitic

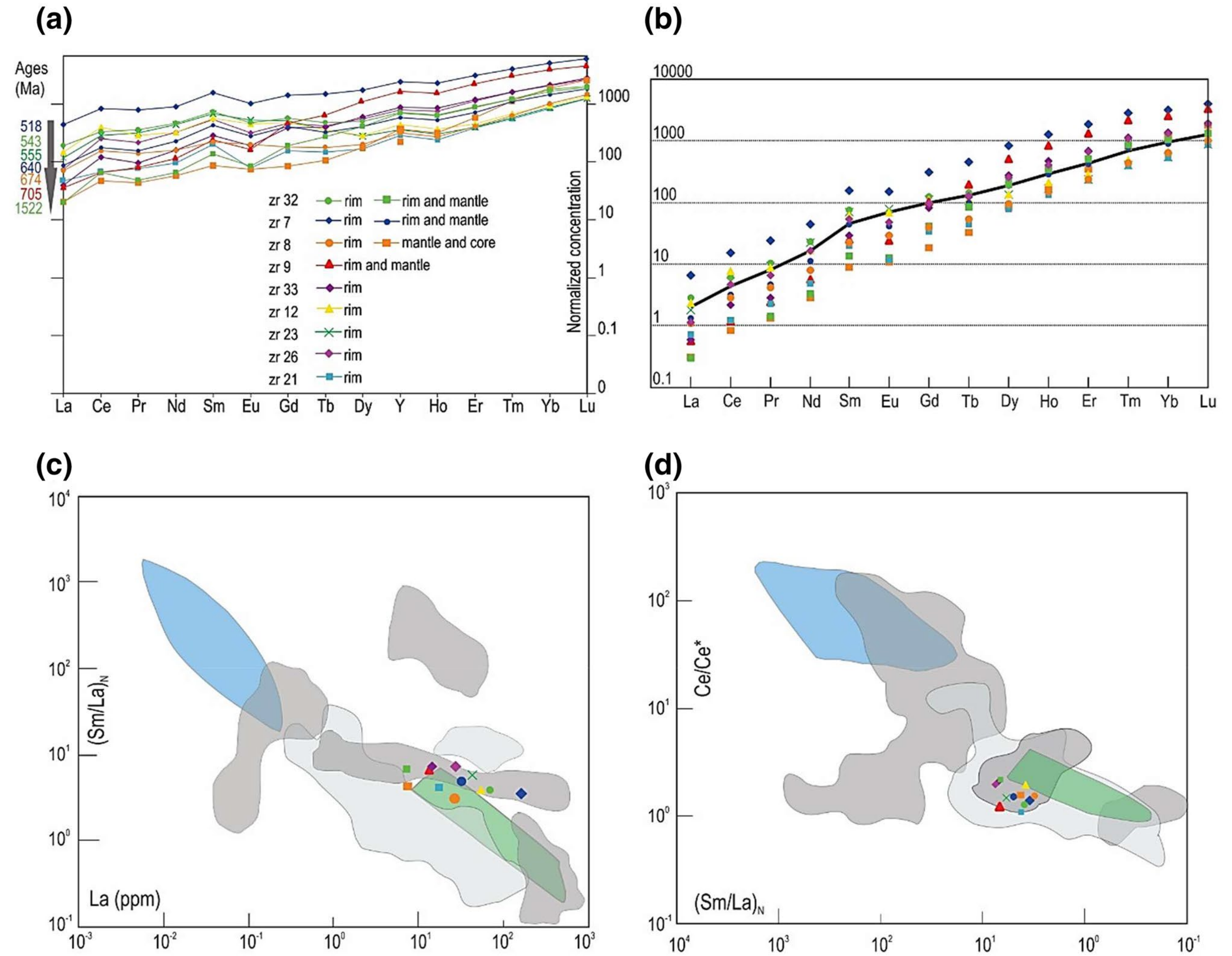

Fig. 14 **a** Chondrite-normalized averaged REE patterns from ROP monzogranite zircons of sample 1 (K-54A) (data from Table 5). Chondrite values are from Taylor and McLennan (1985). **b** Zircon/rock partition coefficients from ROP monzogranite zircons with moving average (data from Table 6). **c**, **d** $(Sm/La)_N$ vs. La and Ce/Ce* vs. (Sm/La)N diagrams. The outlined areas represent the "magmatic" (blue) and "hydrothermal" (green) field defined by Hoskin (2005). Others magmatic (light grey) and hydrothermal (dark grey) fields are from the compilation made by Zhong et al. (2018)

rocks, therefore, not being genetically related to them. However, it can be suggested that the granites of ROP may have derived from reworking of IS rocks of the MC.

The analysed samples from ROP belong to a high-K calc-alkaline series. Granites are slightly peraluminous and quartz microdiorite sample is metaluminous. ROP REE pattern suggests some similarity with A-type post-orogenic rocks, although the REE partition coefficients in zircon crystals are typical from non-A-type granites.

Tectonic implications

Several episodes of amalgamation and subsequent diachronous collision of the terranes and microplates during the closure of the Adamastor Ocean were already postulated by several authors (e.g., Basei et al. 2000, 2009; Heilbron et al. 2008; Brito Neves et al. 1999, 2014 among others).

Table 6 Zircon/rock partition coefficients of REEs, Y, Th, U, Nb, and Ta from the ROP biotite monzogranite—sample 1 (K-54A)

Element	ZR/rock partition											
	WR	ZR 32		ZR7		ZR 8		ZR 9	ZR 33	ZR 12	ZR 23	ZR 26	ZR 21
	K-54A	R1	R2	R3	R4	R5	R6	R7	R8	R9	R10	R11	R12
La	24.36	3	0.3	7	1	1	0.3	1	1	2	2	1	1
Ce	52.60	6	1	15	3	3	1	1	2	7	5	5	1
Pr	4.62	11	1	24	5	4	1	2	3	9	9	6	2
Nd	14.26	23	3	45	11	8	3	6	8	16	22	16	5
Sm	2.29	74	14	157	43	22	9	24	29	58	69	54	20
Eu	0.58	70	13	150	41	29	11	24	29	67	79	48	12
Gd	1.41	124	41	308	88	39	18	100	83	102	110	99	34
Tb	0.19	144	83	449	100	54	32	196	123	111	108	128	45
Dy	0.81	238	194	820	192	95	84	514	278	135	133	258	78
Ho	0.15	352	343	1253	289	151	176	843	466	201	166	408	133
Er	0.42	524	510	1832	424	239	342	1306	693	268	235	665	226
Tm	0.05	850	858	2789	760	440	795	2140	1127	468	404	1107	386
Yb	0.39	1142	1037	3232	915	646	1186	2479	1369	607	556	1328	534
Lu	0.06	1392	1313	4001	1265	1013	1788	3130	1957	927	866	1835	869
Hf	0.0003	4649	4029	5578	5268	5888	4958	4029	4958	4339	5888	5578	6198
Ta	0.48	6	4	25	8	8	1	5	6	4	8	10	8
Th	14.05	37	17	471	25	30	4	32	48	42	44	58	20
U	3.02	395	200	2439	439	731	250	247	473	489	667	738	477
Ti	1978	0.03	0.02	0.11	0.02	0.01	0.04	0.01	0.11	0.07	0.04	0.02	0.01
Y	4.44	361	350	1218	292	161	186	826	447	225	180	403	146
Nb	9.3	1.6	1.0	9.8	1.1	0.9	0.2	0.7	1.3	1.0	0.8	2.2	0.7

R raster and equivalent zircon crystals from Figs. 10 and 13

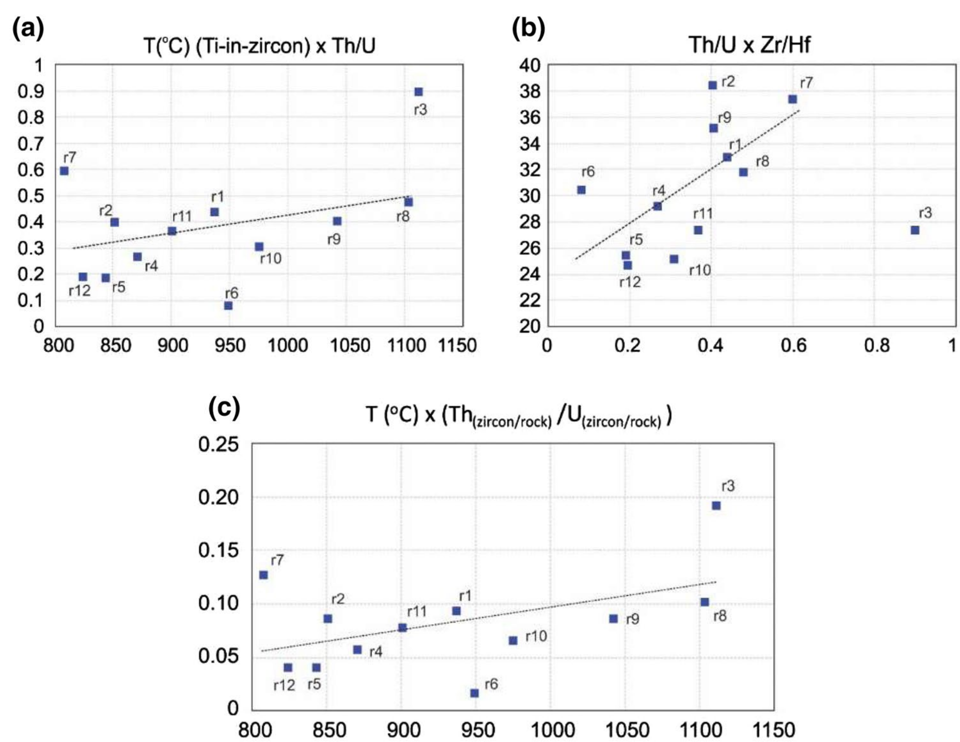

Fig. 15 **a** Ti-in zircon temperature versus Zircon Th/U (sample 1-monzogranite). **b** Zircon Th/U versus Zr/Hf zircon. **c** Plot of fractionation factor ($Th_{(zircon/rock)}/U_{(zircon/rock)}$) versus Ti-in-zircon temperatures. R: raster. The rasters and equivalent zircon crystals are shown in Fig. 15 and Tables 5 and 6

Table 7 Main U–Pb geochronological data of the Mongaguá Complex units

Domain of MC/origin of zircon crystals	Autocrysts crystallization ages	Antecrysts	Neoproterozoic inheritance	Paleo-Mesoproterozoic inheritance
Itariri Suite[a]	745 Ma; 640–630 Ma; 620–612 Ma; 603 Ma	Not available	790 Ma	2.2–2.1 Ga; 1.8 Ga; 1.2–1.1 Ga
Areado Pluton[a]	700 Ma; 2150 Ma	Not available	860 Ma	2.2–2.1 Ga; 1.8 Ga
ROP monzogranite (K-54A—sample 1)	556 Ma (570–540 Ma)	613 Ma; 580 Ma	690 Ma; 645 Ma	2.21 Ga
ROP monzogranite (K-190A—sample 2)	601 Ma	631 Ma; 627 Ma	788 Ma; 682 Ma; 647 Ma (metamorphic rim)	1.9 Ga
ROP quartz diorite (K-190B—sample 3)	624 Ma	655 Ma	684 Ma	2.0 Ga; 1.7 Ga

[a]Data from Passarelli et al. (2014a, 2016)

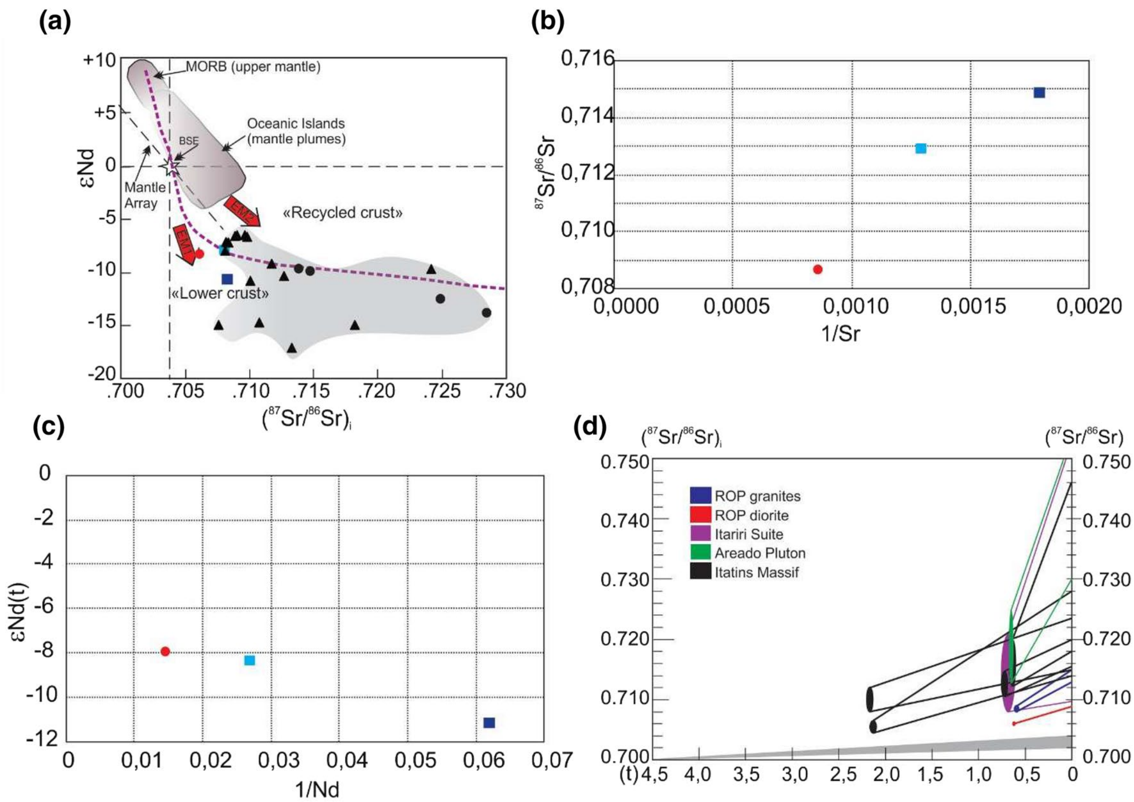

Fig. 16 **a** εNd_i—$(^{87}Sr/^{86}Sr)_i$ diagram (modified after White 2015) for the ROP rocks with initial ratios calculated for 600 Ma: MORB—mid-ocean ridge basalts and BSE–bulk silicate Earth are shown. The mantle sources of MORB and the mantle end-members EMI (enriched mantle type I) and EMII (enriched mantle type II) are from Zindler and Hart (1986). **b** Sr isotope-element mixing diagram. **c** Nd isotope-element mixing diagram. **d** Sr evolution diagram for the MC rocks and charnockitic rocks from the Itatins Complex (Curitiba Terrane). Legend for **a**–**c**: dark-blue square = monzogranite sample 1 (K-54A); light-blue square = monzogranite sample 2 (K-190A); red circle = microdiorite sample-3 (K-190B). Black symbols are of studied rocks of the MC (data from Tables 2 and 3): triangle = Itariri Suite; circle = Areado Pluton

The juxtaposition of Curitiba Terrane (CRT) and Paranapanema craton took place at ca. 630–605 Ma, and of the Luis Alves and CRT was already finished around 590 Ma (Basei et al. 2009). The docking of CoT and adjacent terranes may be occurred subsequently.

One of the deformation phases identified in the Itariri Shear Zone possibly represents an extensional movement resulting from stress release of the juxtaposition of the Embu and Curitiba terranes (Passarelli et al. 2011). Additionally, the wedge configuration of the CoT between the Embu and

Curitiba terranes is due to the sinistral Itariri shear zone movement (Passarelli et al. 2019) which is constrained around 580 Ma (Passarelli et al. 2011, 2019).

The presence of magma mingling/mixing is a common feature in the 580 Ma late- to post-collisional magmatism of the RB (Pedrosa-Soares and Wiedemann-Leonaros 2000; Medeiros et al. 2001; Gualda and Vlach 2007; Meira 2014; Machado et al. 2016), resulting from the intrusion of hot mafic magma into colder felsic magma. On the other hand, the ROP was generated from melting of crustal rocks due the interaction with older hotter mafic magmas at the base of the crust.

The slightly older microdiorite (655–624 Ma) and 613–586 Ma monzogranite in addition to the observed grain-supported flow only in monzogranite and solid-state deformation in both rocks suggest that the initial phases of the mafic magmatism took place under no strain or at an extensional event. Moreover, the continuous closure of the Adamastor Ocean and juxtaposition of the terranes associated with magmatic underplating provided high temperatures of the continental crust for a long-term late orogenic period generating the monzogranite of the ROP under a main compressive tectonic regime.

Conclusions

- Magma mingling between slightly older quartz microdiorite and biotite monzogranite is evidenced in the ROP, where the emplacement of the monzogranite started probably during the medium-to-final stages of crystallization of the quartz microdiorite.
- A hybrid zone between the two magmas is suggested by Nd and Sr isotopic data and by LA-ICP-MS U–Pb zircon geochronology.
- The petrographic analyses indicate syn-tectonic characteristics of the ROP, involving submagmatic and solid-state deformation.
- The petrographic and isotopic analyses indicate that the ROP was produced from partial melting of older crustal rocks, originated probably by underplating of mafic magmas responsible for providing high temperatures of the continental crust during a protracted orogenic evolution of the RB.
- An accurate analysis of LA-ICP-MS U–Pb ages and zircon internal structures allows us to determine a reasonable origin of zircon crystals and the sequence of several magmatic pulses and post-magmatic events over an extended time of 655–556 Ma.

Acknowledgements The authors thank FAPESP (Processes 2013/24316-7 and 2015/03737-0) for the financial support to this work and the Geochronological Research Center (CPGeo) of the Geosciences Institute—USP. We are much grateful to the journal reviewers (Dr. Pradip K. Singh and anonymous) and the Editor-in-Chief; their comments helped us to significantly improve our presentation.

References

Almeida FFM, Hasui Y, Brito Neves BB, Fuck RA (1981) Brazilian structural provinces, an introduction. Earth Sci Rev 17:1–29

Almeida FFM, Brito Neves BB, Carneiro CDR (2000) The origin and evolution of the South American Platform. Earth Sci Rev 50:77–111

Andrade S, Ulbrich HH, Gomes CB, Martins L (2014) Methodology for the determination of trace and minor elements in minerals and fused rock glasses with laser ablation associated with quadrupole inductively coupled plasma mass spectrometry (LA-Q-ICPMS). Am J Anal Chem 5:701–721

Azevedo Sobrinho JM, Janasi VA, Simonetti A, Heaman LM, Santoro J, Diniz HN (2011) The Ilha Anchieta Quartz Monzonite: the southernmost expression of ca. 500 Ma post-collisional magmatism in the Ribeira Belt. An Acad Bras Ciênc 83(3):891–906

Basei MAS, Siga O Jr, Reis Neto JM, Passarelli CR, Prazeres Filho HJ, Kaulfuss G, Sato K, Lima OS (1999) Paleoproterozoic granulitic belts of the Brazilian Southern Region (PR-SC). In: SSAGI, 2, Cordoba, Argentina. Extended abstracts, pp 291–294

Basei MAS, Siga O Jr, Masquelin H, Harara OMM, Reis Neto JM, Preciozzi F (2000) The Dom Feliciano Belt of Brazil and Uruguay and its Foreland Domain the Rio de la Plata Craton: framework, tectonic evolution and correlation with similar provinces of Southwestern Africa. In: Cordani UG, Milani EJ, Thomaz Filho A, Campos DA (eds) Tectonic evolution of South America, Rio de Janeiro, pp 311–334

Basei MAS, Nutman A, Siga O Jr, Passarelli CR, Drukas CO (2009) The evolution and tectonic setting of the Luis Alves Microplate of Southeastern Brazil: an exotic terrane during the assembly of Western Gondwana. In: Gaucher C, Sial AN, Halverson GP, Frimmel HE (eds) Neoproterozoic-Cambrian tectonics, global change and evolution: a focus on southwestern Gondwana. Developments in Precambrian geology, 1st edn. Elsevier, Amsterdam, pp 273–291

Basei MAS, Brito Neves BB, Siga O Jr, Babinski M, Pimentel MM, Tassinari CCG, Hollanda MHB, Nutman A, Cordani UG (2010) Contribution of SHRIMP U Pb zircon geochronology to unravelling the evolution of Brazilian Neoproterozoic fold belts. Precambrian Res 183:112–144

Bouchez JL, Delas C, Gleizes G, Nedelec A, Cuney M (1992) Submagmatic microfractures in granites. Geology 20:35–38

Brito Neves BB, Campos Neto MC, Fuck RA (1999) From Rodinia to Western Gondwana, an approach to the Brasiliano-Pan African Cycle and orogenic collage. Episodes 2:155–166

Brito Neves BB, Fuck RA, Pimentel MM (2014) The Brasiliano collage in South America: a review. Braz J Geol 44(3):493–518

Campanha GAC, Brito Neves BB (2004) Frontal and oblique tectonics in the Brazilian shield. Episodes 27:255–259

Campos Neto MC (2000) Orogenic systems from Southwestern Gondwana, an approach to Brasiliano-Pan African cycle and orogenic collage in Southeastern Brazil. In: Cordani UG, Milani EJ, Thomaz Filho A, Campos DA (eds) Tectonic evolution of South America, international geological congress, 31, Rio de Janeiro, pp 335–365

Cordani UG, Pimentel MM, Ganade de Araújo CE, Basei MAS, Fuck RA, Girardi VAV (2013) Was there an Ediacaran Clymene Ocean in central South America? Am J Sci 313:517–539

Cox KG, Bell JD, Pankhurst RJ (1979) The interpretation of igneous rocks. Allen and Unwin, London

Cury LF, Siga O Jr, Harara OM, Sato K, Basei MAS (2008) Geological and geochronological setting of Paranaguá Domain, Ribeira Belt—Southern Brazil. In: IGC, 33, Oslo. CD-ROM

DePaolo DJ (1981) A neodymium and strontium isotopic study of the Mesozoic calcalkaline granitic batholiths of the Sierra Nevada and Peninsular Ranges, California. J Geophys Res 86:10470–10488

DePaolo DJ, Linn AM, Schubert G (1991) The continental age distribution: methods of determining mantle separation ages from Sm–Nd isotopic data and application to the southwestern United States. J Geophys Res 96:2071–2088

Frimmel HE, Basei MAS, Gaucher C (2011) Neoproterozoic geodynamic evolution of SW-Gondwana: a southern African perspective. Int J Earth Sci Geol Rundsch 100:323–354

Gualda GAR, Vlach SRF (2007) The Serra da Graciosa A-type Granites and Syenites, southern Brazil Part 1: regional setting and geological characterization. An Acad Bras Cienc 79(3):405–430

Harley SL, Kelly NM, Möller A (2007) Zircon behaviour and the thermal histories of mountain chains. Elements 3:25–30

Hawkesworth CJ, Kemp AIS (2006) Using hafnium and oxygen isotopes in zircons to unravel the record of crustal evolution. Chem Geol 226:144–162

Heilbron M, Pedrosa-Soares A, Campos Neto MC, Silva LC, Trouw R, Janasi VA (2004) Brasiliano Orogens in Southeast and South Brazil. In: Weinberg R, Trouw R, Fuck R, Hackspacher P (eds) The 750–550 Ma Brasiliano Event of South America, Journal of the Virtual Explorer Electronic Edition 17: Paper 4

Heilbron M, Valeriano CM, Tassinari CCG, Almeida J, Tupinambá M, Siga O Jr, Trouw R (2008) Correlation of Neoproterozoic terranes between the Ribeira Belt, SE Brazil and its African counterpart: comparative tectonic evolution and open questions. Geol Soc London Spec Publ 294:211–237

Heilbron M, Duarte BP, Valeriano CM, Simonetti A, Machado N, Nogueira JR (2010) Evolution of reworked Paleoproterozoic basement rocks within the Ribeira belt (Neoproterozoic), SE-Brazil, based on U–Pb geochronology: implications for paleogeographic reconstructions of the São Francisco-Congo paleocontinent. Precambrian Res 178:136–148

Heilbron M, Ribeiro A, Valeriano CM, Paciullo FV, Almeida JCH, Trouw RJA, Tupinambá M, Eirado Silva LG (2017) The Ribeira Belt. In: Heilbron M, Cordani UG, Alkmim FF (eds) Regional geology reviews, São Francisco Craton, Eastern Brazil tectonic genealogy of a miniature continent. Springer, Cham, pp 277–304

Hoskin PWO (2000) Patterns of chaos: fractal statistics and the oscillatory chemistry of zircon. Geochim Cosmochim Acta 64:1905–1923

Hoskin PWO (2005) Trace-element composition of hydrothermal zircon and the alteration of hadean zircon from the Jack Hills, Australia. Geochim Cosmochim Acta 69:637–648

Hoskin PWO, Schaltegger U (2003) The composition of zircon and igneous and metamorphic petrogenesis. Rev Mineral Geochem 53(1):27–62

Janasi VA, Alves A, Vlach SRF (2003) Granitos peraluminosos da porção central da Faixa Ribeira, Estado de São Paulo: sucessivos eventos de reciclagem da crosta continental no Neoproterozóico. Geologia USP Série Científica 3:13–24

Kirkland CL, Smithies RH, Taylor RJM, Evans N, McDonald B (2015) Zircon Th/U ratios in magmatic environs. Lithos 212–215:397–414

Košler J, Sylvester PJ (2003) Present trends and the future of zircon in geochronology: laser ablation ICPMS. Rev Mineral Geochem 53(1):243–275

Košler J, Fonneland H, Sylvester P, Tubrett M, Pedersen RB (2002) U–Pb dating of detrital zircons for sediment provenance studies—a comparison of laser ablation ICPMS and SIMS techniques. Chem Geol 182:605–618

Ludwig KR (2012) User's manual for Isoplot 3.75: a geochronological toolkit for Microsoft Excel. Berkeley Geochronology Center Special Publication. http://www.bgc.org/isoplot_etc/isoplot/Isoplot3_75-4_15manual.pdf. Accessed 20 Oct 2019

Machado R, Philipp RP, McReath I, Peucat JJ (2016) Geochemical and isotopic evidence for the petrogenesis and emplacement tectonics of the Serra dos Orgãos batholith in the Ribeira belt, Rio de Janeiro, Brazil. J S Am Earth Sci 68:187–204

Maniar PD, Piccoli PM (1989) Tectonic discrimination of granitoids. Geol Soc Am Bull 101:635–643

Matteini M, Dantas EL, Pimentel MM, Bühn B (2010) Combined U–Pb and Lu–Hf isotope analyses by laser ablation MC-ICP-MS: methodology and applications. An Acad Bras Cienc 82(2):479–491

McDonough WF, Sun SS (1995) The composition of the Earth. Chem Geol 120:223–253

Medeiros SR, Wiedemann-Leonardos CM, Vriend S (2001) Evidence of mingling between contrasting magmas in a deep plutonic environment: the example of Várzea Alegre, in the Ribeira Mobile Belt, Espírito Santo, Brazil. An Acad Bras Cienc 73(1):99–119

Meira VT (2014) Evolução Tectono-Metamórfica Neoproterozoica dos complexos Embu e Costeiro no contexto de formação do Gondwana Ocidental (leste do Estado de São Paulo). Ph.D. Thesis, University of São Paulo

Meira VT, Juliani C, Schorscher JHD, Garcia-Casco A, Hyppolito T (2014) Does the Pico do Papagaio Batholith indeed represent a Neoproterozoic magmatic arc? In: IX South American symposium on isotope geology, abstracts, São Paulo, Brazil

Meira VT, García-Casco A, Juliani C, Almeida RP, Schorscher JHD (2015) The role of intracontinental deformation in supercontinent assembly: insights from the Ribeira Belt, Southeastern Brazil (Neoproterozoic West Gondwana). Terra Nova 27:206–217

Miller JS, Matzel JEP, Miller CF, Burgess SD, Miller RB (2007) Zircon growth and recycling during the assembly of large, composite arc plutons. J Volcanol Geotherm Res 167:282–299

Mori PE, Reeves S, Correia CT, Haukka M (1999) Development of a fused glass disc XRF facility and comparison with the pressed powder pellet technique at Instituto de Geociências, São Paulo University. Rev Bras Geoc 29:441–446

Murphy MA, Salvador A (1999) International stratigraphic guide—an abridged version. International subcommission on stratigraphic classification of IUGS, international commission on stratigraphy. Spec Epis 22(4):255–272

Nakamura N (1974) Determination of REE, Ba, Fe, Mg, Na and K in carbonaceous and ordinary chondrites. Geochim Cosmochim Acta 38:757–775

Navarro MS, Andrade S, Ulbrich H, Gomes CB, Girardi VAV (2008) The direct determination of rare earth elements in basaltic and related rocks using ICP–MS: testing the efficiency of microwave oven sample decomposition procedures. Geostand Res Geoanal 32:167–180

Passarelli CR (2001) Caracterização estrutural e geocronológica dos domínios tectônicos da porção sul-oriental do Estado de São Paulo. Ph.D. Thesis, University of São Paulo

Passarelli CR, Basei MAS, Campos Neto MC, Siga O Jr, Prazeres Filho HJ (2004) Geocronologia e geologia isotópica dos terrenos Pré-cambrianos da porção sul-oriental do Estado de São Paulo. Geologia USP Sér Cient 4:55–74

Passarelli CR, Wemmer K, Siga O Jr, Siegesmund S, Basei MAS (2008) Tectonothermal evolution of the SE São Paulo State Precambrian terranes. In: SSAGI, 6, San Carlos de Bariloche, Argentina. Book of abstracts, p 150

Passarelli CR, Basei MAS, Siga O Jr, Sato K, Sproesser WM, Loios VAP (2009) Dating minerals by ID-TIMS geochronology at times

of in situ analysis: selected case studies from the CPGeo-IGc-USP laboratory. An Acad Bras Cienc 81:1–25
Passarelli CR, Basei MAS, Wemmer K, Siga O Jr, Oyhantçabal P (2011) Major shear zones of southern Brazil and Uruguay: escape tectonics in the eastern border of Rio de la Plata and Paranapanema cratons during the Western Gondwana amalgamation. Int J Earth Sci Geol Rundsch 100:391–414
Passarelli CR, Basei MAS, Siga O Jr (2014a) LA-ICP-MS U–Pb zircon ages and geochemical-isotopic highlights of Mongaguá granitic rocks, Coastal Terrane—Southeastern Brazil. In: Gondwana 15, Madrid. Abstracts book, p 125
Passarelli CR, Siga O Jr, Basei MAS, Szabó G (2014b) Idades LA-ICP-MS do Granito Ribeirão do Óleo–Domínio Mongaguá–Terreno Costeiro–SE do Estado de São Paulo. In: Congresso Brasileiro de Geologia, 47. Anais, Salvador, BA, p 930
Passarelli CR, Basei MAS, Siga O Jr, Silva PMC, Shinoda R (2016) New U–Pb LA-ICP-MS ages from granitic and migmatitic rocks of the Costeiro Terrane, Mongaguá Domain, southeastern Brazil: some petrogenetic implications. In: SSAGI, 10, Puerto Vallarta, México. CD-ROM
Passarelli CR, Verma SK, Mcreath I, Basei MAS, Siga O Jr (2019) Tracing the history from Rodinia break-up to the Gondwana amalgamation in the Embu Terrane, southern Ribeira Belt, Brazil. Lithos 342–343:1–17
Paterson SR, Vernon RH, Tobisch OT (1989) A review of criteria for the identification of magmatic and tectonic foliations in granitoids. J Struct Geol 11:349–363
Paterson SR, Vernon RH, Zak J (2005) Mechanical instabilities and physical accumulation of K-feldspar megacrysts in granitic magma, Tuolumne Batholith, California, USA. J Virtual Explor 18(1):1–18
Pavan M (2017) Modelagem termodinâmica de fusão parcial e metamorfismo em condições de fácies granulito: exemplo do Complexo Itatins, SP. Ph.D. Thesis, University of São Paulo
Peccerillo A, Taylor SR (1976) Geochemistry of eocene calc-alkaline volcanic rocks from the Kastamonu area, northern Turkey. Contrib Mineral Petrol 58:63–81
Pedrosa-Soares AC, Wiedemann-Leonaros CM (2000) Evolution of the Araçuaí Belt and its connection to the Ribeira Belt, Eastern Brazil. In: Cordani UG, Milani EJ, Thomaz Filho A, Campos DA (eds) Tectonic evolution of South America. Secretariat Bureau, 31st International Geological Congress, Rio de Janeiro, pp 265–285
Picanço JL (1994) Aplicação das sistemáticas Sm/Nd e Rb/Sr no Maciço Itatins (SP). Dissertation, University of São Paulo
Picanço JL, Tassinari CCG, Cordani UG, Nutman AP (1998) Idades U–Pb (SHRIMP), Sm–Nd e Rb–Sr em rochas do Maciço de Itatins (SP): evidências de Evolução Policíclica. An Acad Bras Cienc 70:139–150
Rubatto D (2002) Zircon trace element geochemistry: partitioning with garnet and the link between U–Pb ages and metamorphism. Chem Geol 184:123–138
Samperton KM, Bell EA, Barboni M, Keller CB, Schoene B (2017) Zircon age-temperature-compositional spectra in plutonic rocks. Geology 45:983–986
Sato K, Siga O Jr, Silva JA, McReath I, Liu D, Iizuka T, Rino S, Hirata T, Sproesser WM, Basei MAS (2009) In situ isotopic analyses of U and Pb in Zircon by remotely operated SHRIMP II, and Hf by LA-ICP-MS: an example of dating and genetic evolution of zircon by $^{176}Hf/^{177}Hf$ from the Ita Quarry in the Atuba Complex, SE Brazil. Geol USP Sér Cient 9:61–69
Sato K, Basei MAS, Sproesser WM, Siga Jr O (2012) The application of U–Pb geochronology to zircon and titanite by laser ablation—ICP–MS. Geonalysis 2012: the 8th international conference on the analysis of geological and environmental materials, abstracts, p 86
Sato K, Tassinari CCG, Basei MAS, Siga O Jr, Onoe AT, Souza MD (2014) Sensitive high resolution ion microprobe (SHRIMP IIe/MC) of the Institute of Geosciences of the University of São Paulo, Brazil: analytical method and first results. Geologia USP 14(3):3–18
Schmitt RS, Trouw RAJ, Van Schmus WR, Pimentel MM (2004) Late amalgamation in the central part of Western Gondwana: new geochronological data and the characterization of a Cambrian collision orogeny in the Ribeira belt (SE Brazil). Precambrian Res 133:29–61
Siga O Jr, Basei MAS, Reis Neto JM, Machiavelli A, Harara OM (1995) O Complexo Atuba: um cinturão Paleoproterozóico intensamente retrabalhado no Neoproterozóico. Boletim IG-USP Ser Cient 26:69–98
Siga O Jr, Basei MAS, Nutman AP, Sato K, Mcreath I, Passarelli CR, Liu D (2011a) Extensional and collisional magmatic records in the Apiaí Terrane, south-southeastern Brazil: integration of geochronological U–Pb Zircon ages. Geologia USP 11:149–175
Siga O Jr, Cury LF, Mcreath I, Ribeiro LMAL, Sato K, Basei MAS, Passarelli CR (2011b) Geology and geochronology of the Betara Region in South-Southeastern Brazil: evidence for possible Statherian (1.80–1.75 Ga) and Calymmian (1.50–1.45 Ga) extension events. Gondwana Res 19:260–274
Siqueira R, Hollanda MHBM, Basei MAS (2014) A novel approach to (LA-ICP-MS acquired) U–Th–Pb data processing. In: SSAGI, 9, Chile. Program and abstracts, p 306
Stimac JA, Pearce TH (1992) Textural evidence of mafic-felsic magma interaction in dacite lavas, Clear Lake, California. Am Mineral 77:795–809
Sun S, McDonough WF (1989) Chemical and isotopic systematics of oceanic basalts: implications for mantle composition and processes. Geol Soc London Spec Publ 42:313-345
Taylor SR, McLennan SM (1985) The continental crust: its composition and evolution. Blackwell Scientific Publication, Carlton
Trouw RAJ, Heilbron M, Ribeiro A, Pacciullo F, Valeriano CM, Almeida JCH, Tupinambá M, Andreis RR (2000) The central segment of the Ribeira Belt. In: Cordani UG, Milani EJ, Thomaz Filho A, Campos DA (eds) Tectonic evolution of South America. Secretariat Bureau, 31st International Geological Congress, Rio de Janeiro, pp 287–310
Tupinambá M, Heilbron M, Duarte BP, Nogueira JR, Valladares C, Almeida J, Silva LGE, Medeiros SR, Almeida CG, Miranda A, Ragatky CD, Mendes J, Ludka I (2007) Geologia da Faixa Ribeira Setentrional: Estado da Arte e Conexões com a Faixa Araçuaí. Geonomos 15:67–79
Tupinambá M, Heilbron M, Valeriano CM, Porto R Jr, Dios FB, Machado N, Silva LGE, Almeida JCH (2012) Juvenile contribution of the Neoproterozoic Rio Negro Magmatic Arc (Ribeira Belt, Brazil): implications for Western Gondwana amalgamation. Gondwana Res 21:422–438
Vaughan APM, Pankhurst RJ (2008) Tectonic overview of the West Gondwana margin. Gondwana Res 13:150–162
Vernon RH (1991) Interpretation of microstructures of microgranitoid enclaves. In: Didier J, Barbarin B (eds) Enclaves and granite petrology, developments in petrology, vol 13. Elsevier, Amsterdam, pp 277–291
Vernon RH (2000) Review of Microstructural evidence of magmatic and solid-state flow. Electron Geosci 5:2
Vernon RH, Paterson SR (2006) Mesoscopic structures resulting from crystal accumulation and melt movement in granites. Trans R Soc Edinb Earth Sci 97:369–381
Wang X, Chen J, Ren M (2016) Hydrothermal zircon geochronology: age constraint on Nanling Range tungsten mineralization (Southeast China). Ore Geol Rev 74:63–75
White WM (2015) Isotope geochemistry. Wiley, Oxford
Wu FY, Yang YH, Xie LW, Yang JH, Xu P (2006) Hf isotopic composition of the standard zircons and baddeleyites used for U–Pb geochronology. Chem Geol 234:105–126

Zhong S, Feng C, Seltmann R, Li D, Qub H (2018) Can magmatic zircon be distinguished from hydrothermal zircon by trace element composition? The effect of mineral inclusions on zircon trace element composition. Lithos 314–315:646–657

Zindler AW, Hart SR (1986) Chemical geodynamics. Annu Rev Earth Planet Sci 14:493–571